

A mid-IR study of Hickson Compact Groups

II. Multi-wavelength analysis of the complete GALEX-Spitzer Sample

T. Bitsakis¹, V. Charmandaris^{1,2,3}, E. da Cunha⁴, T. Díaz-Santos¹, E. Le Floch⁵, and G. Magdis⁶

¹ Department of Physics & ICTP, University of Crete, GR-71003, Heraklion, Greece

² IESL/Foundation for Research & Technology-Hellas, GR-71110, Heraklion, Greece

³ Chercheur Associé, Observatoire de Paris, F-75014, Paris, France

⁴ Max Planck Institute für Astronomie, D-69117, Heidelberg, Germany

⁵ Laboratoire AIM, CEA/DSM - CNRS - Université Paris Diderot, IRFU/Service d'Astrophysique, F-91191, Gif-sur-Yvette Cedex, France

⁶ University of Oxford, Department of Physics, Keble Road, Oxford OX1 3RH, UK

Preprint online version: November 27, 2021

ABSTRACT

We present a comprehensive study on the impact of the environment of compact galaxy groups on the evolution of their members using a multi-wavelength analysis, from the UV to the infrared, for a sample of 32 Hickson compact groups (HCGs) containing 135 galaxies. Fitting the SEDs of all galaxies with the state-of-the-art model of da Cunha (2008) we can accurately calculate their mass, SFR, and extinction, as well as estimate their infrared luminosity and dust content. We compare our findings with samples of field galaxies, early-stage interacting pairs, and cluster galaxies with similar data. We find that classifying the groups as dynamically “old” or “young”, depending on whether or not at least one quarter of their members are early-type systems, is physical and consistent with past classifications of HCGs based on their atomic gas content. Dynamically “old” groups are more compact and display higher velocity dispersions than “young” groups. Late-type galaxies in dynamically “young” groups have specific star formation rates (sSFRs), NUV-r, and mid-infrared colors which are similar to those of field and early stage interacting pair spirals. Late-type galaxies in dynamically “old” groups have redder NUV-r colors, as they have likely experienced several tidal encounters in the past building up their stellar mass, and display lower sSFRs. We identify several late-type galaxies which have sSFRs and colors similar to those of elliptical galaxies, since they lost part of their gas due to numerous interactions with other group members. Also, 25% of the elliptical galaxies in these groups have bluer UV/optical colors than normal ellipticals in the field, probably due to star formation as they accreted gas from other galaxies of the group, or via merging of dwarf companions. Finally, our SED modeling suggests that in 13 groups, 10 of which are dynamically “old”, there is diffuse cold dust in the intragroup medium. All this evidence point to an evolutionary scenario in which the effects of the group environment and the properties of the galaxy members are not instantaneous. Early on, the influence of close companions to group galaxies is similar to the one of galaxy pairs in the field. However, as the time progresses, the effects of tidal torques and minor merging, shape the morphology and star formation history of the group galaxies, leading to an increase of the fraction of early-type members and a rapid built up of the stellar mass in the remaining late-type galaxies.

Key words. Infrared: galaxies — Galaxies: evolution — Galaxies: interactions — Galaxies: star formation

1. Introduction

It has become increasingly evident that interactions and merging of galaxies have contributed substantially to their evolution, both in terms of their stellar population as well as their morphological appearance. Compact galaxy groups, with their high galaxy density and signs of tidal interactions among their members, are ideal systems to study the impact on environment to the evolution of galaxies. The Hickson Compact Groups (HCGs) are 100 systems of typically 4 or more galaxies in a compact configuration on the sky (Hickson 1982). They contain a total of 451 galaxies and are mostly found in relatively isolated regions where no excess of surrounding galaxies can be seen, reflecting a strong local density enhancement. The HCGs occupy a unique position in the framework of galaxy evolution, bridging the range of galaxy environments, from field and loose groups to cores of rich galaxy clusters. The fact that the original selection

of the HCG members did not include redshift information, led to the inclusion of interlopers among them, the most famous being NGC 7320 in Stephan’s Quintet (HCG 92). This led to a debate as to whether compact groups are line-of-sight alignments of galaxy pairs within loose groups, or filaments seen end-on (Mamon 1986; Hernquist et al. 1995). However, the detection of hot X-ray gas in ~75% of the HCGs by Ponman et al. (1996) implies that they reside in a massive dark matter halo and thus are indeed physically dense structures. Numerical simulations indicate that in the absence of velocity information, raising the minimum surface brightness criterion for the group used by Hickson would help eliminate interlopers (see McConnachie et al. 2008).

Because of the nature of these groups, the high density enhancements in addition to the low velocity dispersions (~250 km s⁻¹), make them ideal to study the effects of galaxy interactions. Hickson (1982) found that the majority of HCGs display an excess of elliptical galaxies, ~31% of all members compared to the field, while the fraction of spiral galaxies and irregular is only 43%, nearly a factor of two less of what is observed

Send offprint requests to: T. Bitsakis, e-mail: bitsakis@physics.uoc.gr

in the field. Optical imaging by Mendes de Oliveira & Hickson (1994) showed that 43% of all HCG galaxies display morphological features of interactions and mergers, such as bridges, tails and other distortions. Similar indications of interactions are seen in maps of the atomic hydrogen distribution in selected groups by Verdes-Montenegro et al. (2001). Moreover, Hickson (1989) found that the fractional distribution of the ratio of far-infrared (far-IR) to optical luminosity in HCG spiral galaxies is significantly larger than that of isolated galaxies, suggesting that for a given optical luminosity, spiral galaxies in groups have higher infrared luminosities. Comparison of HCG spirals with those in clusters of galaxies from Bica & Giovanelli (1987) reveals that the distributions of the IR to optical luminosity, as well as the 60 to 100 μ m far-IR color are similar. Finally, nuclear optical spectroscopy studies indicate that almost 40% of the galaxies within these groups display evidence of an active galactic nucleus (AGN, Martinez et al. 2010; Shimada et al. 2000). All these clues are consistent with an evolutionary pattern where tidal encounters and the accretion of small companions by the group members, redistribute the gas content of the groups and affect the morphology of their members.

Verdes-Montenegro et al. (2001) and Borthakur et al. (2010) have proposed an evolutionary sequence for the HCGs based on the amount and spatial distribution of their neutral atomic gas. Using HI maps they classified the groups into three phases based on the ratio of the gas content within the galaxies over the total observed in the group. According to their scenario, a loose galaxy group starts to contract under the gravity to form a more compact one. During this first phase the HI gas is still mostly found in the individual galaxies. Then as the group evolves, it enters the second phase and a fraction of the atomic hydrogen is extracted from the galaxy disks into the intragroup medium, probably due to tidal forces, and part of it becomes fully ionized. Finally, in the third phase, the dynamical friction leads to a decrease in the separation between the group members and the group becomes more compact. More than 80% of the HI originally in the disks of the galaxies has been displaced. Some of it is seen redistributed in a common envelope surrounding all groups members, and a fraction has likely been converted into molecular gas fueling star formation and/or accretion onto an AGN. A similar classification was proposed by Johnson et al. (2007) and Tzanavaris et al. (2010). These authors separated the groups using the ratio of the M_{HI} over the dynamical mass of the group, the so-called “HI richness”, and found that it is correlated to the specific star formation (sSFR) of their galaxies. They also found that galaxies in gas-poor groups display colors representative of a normal stellar population and observed a bimodality in the mid-infrared colors, as well as in the sSFRs of their members. They suggested that this is caused by enhanced the star formation activity which lead the galaxies in groups to evolve faster. Walker et al. (2010) had concluded that a similar bimodality in the mid-IR is also observed in the colors of galaxies in the Coma Infall region.

A necessary step to determine the evolutionary state of HCGs, is the analysis of not just the morphology of the group members, but of their stellar population and star formation history. In our first paper (Bitsakis et al. 2010), we commenced exploring the properties of an initial sample of 14 HCGs in mid-IR wavelengths and found that a large fraction of the early type galaxies in groups, have mid-IR colors and spectral energy distributions (SEDs) consistent with those of late-type systems. We suggested that this possibly stems from an enhanced star formation, as a result of accretion of gas rich dwarf companions. We found no evidence that the star formation rate (SFR) and built up

of stellar mass of late-type galaxies in groups is different from what is observed in early-stage interacting pairs, or spiral galaxies in the field. However, when we separated the groups according to the fraction of their early type members, they appear to differentiate from the control samples. This would suggest an evolutionary separation of HCGs and can provide a better insight on the nature of these groups.

Despite the progress in the analysis of the properties of these groups, there are still several open questions. Is the bimodality of the mid-IR colors and sSFRs indeed linked with the evolutionary sequence of these galaxies, or it is also observed in other galaxies? How do the properties of HCG galaxies compare to those of galaxies in other environments? Is it really physical to classify the evolutionary stages of these groups also according to the fraction of their early-type systems? Is this classification meaningful in terms of galaxy properties and colors and does it agree with the other classifications? To answer these questions we need multi-wavelength data, as well as a theoretical model to fit their global SED, in order to obtain the best possible constraints on the physical parameters. In this paper we present the first such analysis for a large sample, nearly one third of all Hickson groups, for which we have retrieved observations from the UV to the infrared part of the spectrum.

The structure of the paper is the following. We present our samples, the observations and the data reduction in Section 2. In Section 3, we describe the model used to fit the data as well as the basic physical parameters we can derive, along with their uncertainties. Our results are shown in Section 4, and our conclusions are summarized in Section 5. In an Appendix we provide additional information on 10 early-type galaxies which have peculiar mid-IR colors and SEDs.

2. Observations and Data Reduction

Our sample was constructed from the original Hickson (1982) catalogue of 100 groups, using as criterion the availability of high spatial resolution 3.6 to 24 μ m mid-infrared imagery from the Spitzer Space Telescope archive, as well as UV imaging from GALEX. The infrared data are essential to probe the properties of the energy production in nuclei of galaxies, some of which may be enshrouded by dust, while the UV is necessary to properly estimate the effects of extinction and accurately account for the global energy balance when we model their SED. These constraints resulted in a sample of 32 compact groups containing 135 galaxies, 62 (46%) of which are early-type (E’s & S0’s) and 73 (54%) are late-type (S/SB’s & Irr’s). This nearly triples the sample of 14 HCGs we studied in Bitsakis et al. (2010). We verified that all galaxies of the groups are sufficiently separated in order to be able to obtain accurate photometry from the UV to the mid-IR, and that the average group properties such as type of galaxy, stellar mass, star formation rates are representative of the whole Hickson sample. We should note that 7 groups contain interlopers along the line of sight. For these groups the number of physical members is three, below the lower limit of four members introduced by Hickson (1982). In Table 1 we present a summary of all observations available. The complete photometry is presented in Table 2.

2.1. GALEX data

The UV data presented in this paper were obtained from the Galaxy Evolution Explorer (GALEX) All Sky Survey (AIS), the Medium Imaging Survey (MIS), as well as from Guest Investigator Data publicly available in the GALEX archive.

GALEX is a 50cm diameter UV telescope that images the sky simultaneously in both FUV and NUV channels, centered at 1540Å and 2300Å, respectively. The field of view (FOV) is approximately circular with a diameter of 1.2° and a resolution of about $5.5''$ (FWHM) in the NUV. The data sets used in this paper are taken from the GALEX sixth data release (GR6). More technical details about the GALEX instruments can be found in Morrissey (2005). We performed aperture photometry and carefully calculated the isophotal contours around each source to account for variations in the shape of the emitting region, since most of the sources have disturbed morphologies. By examining the local overall background for each galaxy, we defined a limiting isophote 3σ above it and we measured the flux within the region, after subtracting the corresponding sky. Finally, the conversion from counts to UV fluxes was done using the conversion coefficients given in the headers of each file. Our measurements are presented in Table 2.

2.2. SDSS-Optical data

We compiled the B and R band images of all the galaxies in our sample as reported in Table 2 of Hickson (1989), who had observed the groups for 200s in both B and R bands using FOCAS1 on the Canada French Hawaii telescope resulting in images of $0.42''$ pixel $^{-1}$ and a typical resolution of $1.2''$ (FWHM). In addition, imaging data of 74 galaxies in the u, g, r, i, z bands, centered at 3557, 4825, 6261, 7672 and 9097Å respectively, were recovered from the Sloan Digital Sky Survey (SDSS). We used the SDSS DR7 “model magnitudes”, which reflect the integrated light from the whole galaxy and are best suited for comparisons with total photometry from ultraviolet to infrared wavelengths.

Furthermore, optical spectra were available for 94 galaxies, 70% of our sample. Using the BPT diagram, Martinez et al. (2010) classified the nuclei of 67 galaxies in our sample, while the remaining were obtained from Shimada et al. (2000), Hao et al. (2005) and Véron-Cetty & Véron (2006). The results are shown in Table 2. Galaxies without emission are referred as “unclas.” (unclassified), as they display only stellar absorption features, “HII” are the galaxies with a starburst nucleus, “AGN” (or LINER & Sy2) are the ones with an active nucleus. A number of galaxies are classified as transition objects (TO) since their emission line ratios are intermediate between Kauffmann et al. 2003 and Kewley et al. 2006 criteria. Based on these results for the galaxies in our sample where nuclear classification was available, 37% host an AGN, which is close to the 40% which Martinez et al. (2010) and Shimada et al. (2000) found for their samples.

2.3. Near-Infrared Observations

Deep near-IR observations were obtained for 15 of the groups, using the Wide Field Infrared Camera (WIRC) of the 5m Hale telescope at Palomar. As we discussed in Bitsakis et al. (2010) all groups were imaged in the J, H, and Ks bands for an on-source time of 20 minutes per filter (Slater et al. 2004). Source extraction was performed with SExtractor (Bertin & Arnouts 1996). Our 1σ sensitivity limit was ~ 21.5 mag arcsec $^{-2}$ in J and H bands and ~ 20.5 mag arcsec $^{-2}$ for Ks. For the remaining 17 groups of our sample, the near-IR fluxes were obtained from the Two Micron All Sky Survey (2MASS; Skrutskie et al. 2006). In cases where the proximity of galaxy pairs was affecting the reliability of the 2MASS photometry, we used the reduced 2MASS images and performed aperture photometry ourselves defining

the same aperture we used in other wavelengths. However, for HCG6 the 2MASS photometry was problematic and we observed the group using the wide-field near-IR camera of the 1.3m telescope at Skinakas Observatory, in Crete (Greece). The observations were carried out between 21 and 23 of September 2010. The group was imaged in the J, H and Ks bands for an on-source time of 30min per filter and flux calibration was performed using the a set of near-IR standard stars. Data reduction and aperture photometry was performed using IDL specialized routines. All near-IR photometry for our sample is available in Table 2.

2.4. Mid-Infrared Spitzer Observations

Mid-IR observations for 11 of the groups were performed by us, using Spitzer Space Telescope between 2008 January and 2009 March. We used the Infrared Array Camera (IRAC, Fazio et al. 2004) and obtained 270sec on-source exposures with the 3.6, 4.5, 5.8 and $8.0\mu\text{m}$ broadband filters. Each group was also imaged with the Multiband Imaging Photometer for Spitzer (MIPS, Rieke et al. 2004) with a 375.4sec on source exposure at $24\mu\text{m}$. Details on the analysis of these data were presented in Bitsakis et al. (2010). The Spitzer mid-IR fluxes for 8 more groups of the sample were obtained from Johnson et al. (2007). In brief, the IRAC observations were taken in high dynamic range with 270 or 540sec exposures depending on the group. MIPS $24\mu\text{m}$ images were obtained by the same authors with exposures of 180 or 260sec duration for the same reason. Finally, for 13 groups we recovered the IRAC and MIPS $24\mu\text{m}$ data from the Spitzer archive (PIDs: 159; 198; 50764; 40385) and reduced them as in Bitsakis et al. (2010). The details of these observations are presented in Table 3, and the compilation of all mid-IR measurements is included in Table 2.

2.5. Far-Infrared data

Integrated far-IR photometry at 60 and $100\mu\text{m}$ data for each group as a whole, was obtained from Allam et al. (1996). However, because of the compact environment and small angular separation of the galaxies in the HCGs, the coarse angular resolution of IRAS at the 60 and $100\mu\text{m}$ ($\sim 100''$), enabled us to resolve only 31 individual galaxies of our sample which were sufficiently isolated and bright.

Using the recently released AKARI data we retrieved far-IR observations for 26 galaxies of our sample (22 of them were common with the IRAS sample), which were obtained with the Far-IR Surveyor (FIS) and processed with the AKARI official pipeline software version 20080530 (Okada et al. 2008). The photometry using N60, WIDE-S, WIDE-L, and N160 filters, centered at 65, 90, and 140 $160\mu\text{m}$ was downloaded from the AKARI on-line archive and is reported along with the IRAS data on Table 2. We should note that the FWHMs of the AKARI PSF is $\sim 45''$ at 65 and $90\mu\text{m}$ and $\sim 60''$ at 140 and $160\mu\text{m}$. Even though this is better than IRAS, as we will discuss in more detail later, it places restrictions in interpreting the far-IR properties of the groups and the spatial distribution of their cold dust content.

2.6. Comparison Samples

In order to put the properties and evolution of the group galaxies into context, we must compare their observables and derived physical parameters with other control samples. Since dynamical interactions are the main drivers of galaxy evolution, we examined isolated field galaxies, as well as systems which are

dynamically interacting, such galaxy pairs and galaxies found in clusters for which we could obtain data of similar wavelength coverage. The samples we used in our analysis are the following:

2.6.1. Isolated Field Galaxies

A well studied sample with superb data coverage is the 75 “normal”, mostly isolated field galaxies from the Spitzer Infrared Nearby Galaxies Survey (SINGS; Kennicutt et al. 2003; Dale et al. 2005). We should note that the SINGS sample was selected explicitly to cover a wide range in Hubble type and luminosity and as a result it is not characteristic of a volume or flux limited population. Most objects are late-type systems that have angular sizes between $5'$ and $15'$. It also contains four early-type galaxies (NGC 855, NGC 1377, NGC 3773, and NGC 4125) with the last one being a LINER. Since the SINGS sample does not have many early type galaxies, we used the 9 isolated early-type galaxies with available mid-IR imaging described in Temi et al. (2004) and expanded it with another 4 isolated galaxies (NGC1404, NGC1199, NGC5363 & NGC5866) for which Spitzer mid-IR imaging was also available.

2.6.2. Interacting Galaxy Pairs

This sample is drawn from the 35 nearby ($v < 11,000 \text{ km s}^{-1}$) early stage interacting galaxy pairs of Smith et al. (2007a). The galaxies are tidally disturbed and fairly extended, having linear sizes $> 3'$. For the purposes of this work only 26 pairs from the initial sample were used, in which all the data were available. As discussed in Bitsakis et al. (2010), the stellar mass distributions are similar between this sample as well ours and the SINGS.

2.6.3. Field, Group, and Cluster galaxies

To compare in more detail the UV-optical colors of the galaxies in HCGs with the colors of galaxies found in the field, as well as in other groups and clusters, we used the volume limited sample of Haines et al. (2008). This sample contains 1994 galaxies in redshift range $0.005 \leq z \leq 0.037$, selected by cross-correlating the SDSS-DR4 sample with the GALEX GR3 photometric catalogues. Using the $H\alpha$ equivalent widths of $M_r < -18$ galaxies the authors were able to separate the galaxies into passively evolving and star-forming, having $EW(H\alpha) < 2$ and $EW(H\alpha) > 2$ respectively. To quantify the effects of local mass density and environment the authors calculated the local galaxy number density, ρ , in units of projected area, in Mpc^2 , around a central galaxy and within a radial velocity bin of 500 km s^{-1} . They found that for $\rho < 0.5 \text{ Mpc}^{-2} (500 \text{ km s}^{-1})^{-1}$ they can produce a pure field sample. If a galaxy has $\rho > 4.0 \text{ Mpc}^{-2} (500 \text{ km s}^{-1})^{-1}$ there is a 90% probability that it lies within the virial radius of a group or a cluster.

3. Estimating the physical parameters of the galaxies

3.1. Fitting the UV, Optical, and IR SEDs

We use the state-of-the-art physically motivated model of da Cunha et al. (2008)¹, to fit the SEDs of the galaxies in our sample. As discussed in detail by da Cunha et al. (2008) the model assumes that the source of energy in a galaxy is due to

¹ The da Cunha et al. (2008) model is publicly available at <http://www.iap.fr/magphys>.

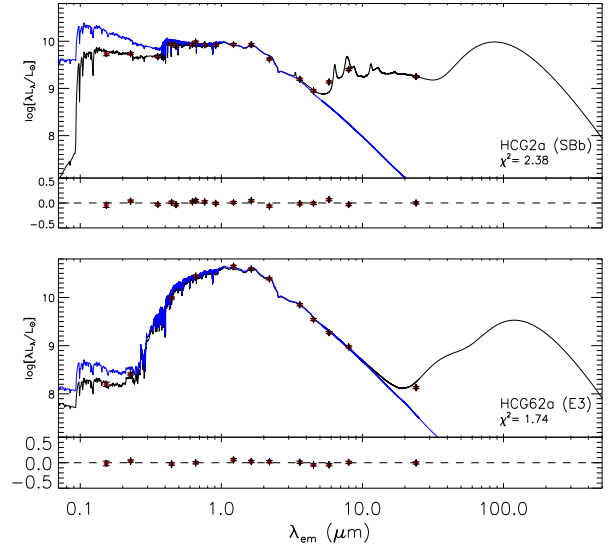


Fig. 1. Example of best fit models (in black line) to the observed spectral energy distributions of two galaxies of our sample. One is a typical late-type galaxy (HCG2a; top panel) and the second is a quiescent elliptical galaxy (HCG62a; bottom panel). In each panel, the blue line shows the unattenuated stellar spectrum estimated by the model. The red circles are the observed broad-band luminosities with their errors as vertical bars. The residuals, $(L_{\lambda}^{\text{obs}} - L_{\lambda}^{\text{mod}})/L_{\lambda}^{\text{obs}}$, are shown at the bottom of each panel. Note the uncertainty in the far-IR shape of the SED due to lack of high spatial resolution data.

an ensemble of stellar populations (no AGN heating is included) whose emission is partially absorbed by dust and re-emitted at longer wavelengths. The model treats the complete SED from the UV to the far-IR and allows us to derive not simply best fit physical parameters to the data, but also to provide the range of their median-likelihood values which are consistent with the observations. To achieve this, the model adopts a Bayesian approach which draws from a large library of random models encompassing all plausible parameter combinations, such as star formation histories, metallicities, dust optical depths as well as dust masses and temperatures. Clearly the wider the wavelength coverage, the more robust the derived parameters. Thus to properly estimate the effect of dust extinction, the UV and optical range needs to be well sampled, while to estimate dust masses and luminosities mid- and far-IR coverage is essential. In addition to the HCG sample, we used the model to fit the interacting pairs of Smith et al. (2007a) and the results are presented in the Table 5. The galaxies of the SINGS sample had already been fit by da Cunha et al. (2008).

3.1.1. Description of the model

The da Cunha et al. (2008) model computes the emission by stars in galaxies using the latest version of the Bruzual & Charlot (2003) population synthesis code. This code predicts the spectral evolution of stellar populations in galaxies from far-ultraviolet to infrared wavelengths and at ages between 1×10^5 and 1.37×10^{10} yr, for different metallicities, initial mass functions (IMFs) and star formation histories. In this work, we adopt the Chabrier (2003) Galactic-disc IMF. The model does not take in account the energy contribution of an active nucleus

to the global SED. Since nearly 40% of our sources host an optically identified AGN one could consider that this could introduce a bias in our analysis. However, based on a number of mid-IR diagnostics the influence of the active nucleus to the total infrared emission of the majority of our galaxies is insignificant, thus this limitation does not affect seriously our conclusions (see details in Section 4.5).

The emission from stars is attenuated using a two component dust model of Charlot & Fall (2000). This model uses an “effective absorption” curve for each component. They use this prescription to compute the total energy absorbed by dust in the birth clouds (BC) and in the ambient interstellar medium (ISM); this energy is re-radiated by dust at infrared wavelengths. They define the total dust luminosity re-radiated by dust in the birth clouds and in the ambient ISM as L_d^{BC} and L_d^{ISM} , respectively. The total luminosity emitted by dust in the galaxy is then $L_d^{tot} = L_d^{BC} + L_d^{ISM}$. The value of L_d^{BC} and L_d^{ISM} is calculated over the wavelength range from 3 to 1000 μm using four main components:

- The emission from polycyclic aromatic hydrocarbons (PAHs; i.e. mid-infrared emission features).
- The mid-infrared continuum emission from hot dust with temperatures in the range 130-250 K.
- The emission from warm dust in thermal equilibrium with adjustable temperature in the range 30-60 K.
- The emission from cold dust in thermal equilibrium with adjustable temperature in the range 15-25 K.

A detail analysis of da Cunha et al. (2008) suggests that the above minimum number of components is required to account for the infrared spectral energy distributions of galaxies in a wide range of star formation histories.

3.1.2. Model library

We use a large random library of star formation histories and dust emission models presented in da Cunha et al. (2008). In this library, each star formation history is parameterized using a star formation rate that is exponentially declining with time, on top of which random bursts are superimposed. The metallicities of these models are sampled uniformly between 0.2 and 2 times solar, and the model ages are distributed uniformly between 0.1 and 13.5 Gyr. Each stellar emission model computed using these star formation histories, ages and metallicities is then attenuated by dust using the two-component description of Charlot & Fall (2000) described above, using a wide range of V-band dust optical depths in the birth cloud and ISM component. Each of these model spectra are then consistently connected to dust emission spectra spanning a wide range in dust temperatures and fractional contributions of each dust emission component to the total dust luminosity. In particular, dust emission models with the same dust luminosity and the same relative contributions to total dust luminosity from the birth cloud and ISM (i.e. L_d^{tot} and f_μ) are assigned to each stellar emission model, as detailed in da Cunha et al. (2008).

For each ultraviolet to infrared model spectrum in this library, we compute the synthetic photometry in the GALEX FUV and NUV, SDSS ugriz, B, R, near-IR, Spitzer IRAC and MIPS-24, AKARI/FIS and IRAS 60 and 100 μm bands at the redshifts of our galaxies to allow for a direct comparison between the observed and model broad-band SEDs as detailed below.

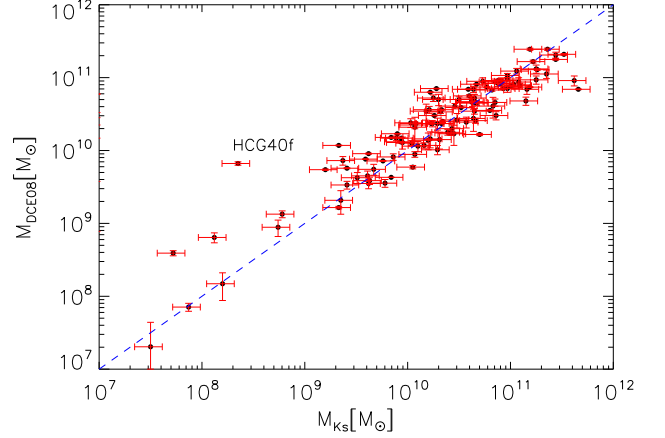


Fig. 2. Stellar masses based on the da Cunha et al. (2008) model (hereafter M_{DCE08}) are plotted as a function of the ones derived from Bell et al. (2003) relation based on Ks luminosity (M_{Ks}) after applying the corrections discussed in the text. Vertical error bars indicate the 16-84 percentile ranges in the recovered probability distributions while the horizontal error bars are the 30% errors of Bell et al. (2003) due to uncertainties in the star formation history and dust. The blue dashed line represents the one-to-one relation.

3.1.3. Spectral fits

We compare the observed spectral energy distributions of the galaxies in our HCGs to every model in the stochastic library of models described above by directly comparing the observed and model broad-band fluxes and computing the χ^2 goodness of fit for each model in the library. This allows us to compute, for each galaxy in the sample, the full likelihood distributions of several model parameters, such as the star formation rate, stellar mass, V-band optical depth in the birth clouds and ISM, dust luminosity etc. We take our final estimate of each parameter to be the median of the likelihood distribution, and the associated confidence interval to be the 16th – 84th percentile range of that distribution.

As examples of our fits, we show in Fig. 1 the best-fit spectral energy distributions of two galaxies from our sample: one quiescent, moderately dusty galaxy (HCG48a, bottom panel); and one actively star-forming, relatively dusty galaxy (HCG7a, top panel).

We note that, as discussed in Sect. 2, even though far-IR measurements are available for each HCG as a whole, most of the galaxies are not independently resolved in the far-IR, due to the large IRAS beam sizes. This presents a serious limitation to the sampling of our SEDs and consequently to the constraints on the dust temperature, total dust mass and luminosity of each galaxy. One of the strengths of this approach is that, by building the full likelihood distributions of the model parameters, we are able to take these uncertainties caused by the lack of far-IR observations into account (see also da Cunha et al. 2008).

3.2. Comparison of empirical to model results

Given the available observations, the stellar mass and star formation rate (SFR) of a galaxy are the two physical parameters which are constrained more accurately using our SED mod-

elling. Since in Bitsakis et al. (2010) we did not had the multi-wavelength data and the model, we used semi-empirical methods, relying on the K-band luminosity and the $24\mu\text{m}$ emission, to estimate the stellar mass and the SFR respectively. In this section, we compare the model derived parameters with those from the empirical methods, to better understand the uncertainties in the interpretation of the results. We also compare them with the methods of Salim et al. (2007) and Iglesias-Páramo et al. (2006), which use the NUV and FUV bands of GALEX, respectively, to estimate the SFR, in order to evaluate their consistency with the model results.

The stellar mass of a galaxies can be estimated using the Bell et al. (2003) prescription which was calibrated using a large sample of galaxies in the local universe. Their formula, based on the K-band luminosity, is:

$$M(M_{\odot}) = 10^{a+b(B-R)} \times L_{Ks}(L_{Ks,\odot}) \quad (1)$$

where B and R are the B- and R-band magnitudes of the galaxy, L_{Ks} its Ks-band luminosity in units of solar luminosities ($L_{Ks,\odot} = 4.97 \times 10^{25} \text{W}$), $a = -0.264$, and $b = 0.138$, with systematic errors of $\sim 30\%$ due to uncertainties in the star formation history and dust. Because these authors used “diet” Salpeter IMF, we corrected it to a Chabrier IMF (which our model uses). Finally, we applied the color correction described in Zibetti et al. (2009) for the Charlot & Bruzual 2007 libraries (CB07), where a is -1.513 and b is 0.750 for the same colors. As we can see in Fig. 2, the masses estimated by the model (M_{model}) agree with the Zibetti et al. (2009) ones. This was somewhat expected as the latter recipe was calibrated using the same models. However, there are some outliers such as HCG40f, for which the model was not able to estimate very well the stellar mass since there were not enough observations to well constrain its SED.

The rate by which a galaxy forms stars, is one of its most important properties, especially in interacting systems which evolve very rapidly as they consume the available gas. In the absence of narrow band imaging of the hydrogen recombination lines (i.e. $H\alpha$), two of the most common ways to estimate the SFR rely on prescriptions using their UV broad band emission from GALEX or the $24\mu\text{m}$ thermal dust emission from Spitzer/MIPS.

Since a significant fraction of the bolometric luminosity of a galaxy is absorbed by interstellar dust and re-emitted in the thermal IR, mid-IR observations can probe the dusty interstellar medium and dust-enshrouded SFRs. The efficiency of the IR luminosity as a SFR tracer depends on the contribution of young stars to heating of the dust and the optical depth of the dust in the star forming regions. Calzetti et al. (2007) using a wealth of multi-wavelength observations for 33 SINGs galaxies provided the following recipe:

$$\text{SFR}_{24}(M_{\odot}\text{yr}^{-1}) = 1.27 \times 10^{-38} (L_{24}(\text{erg s}^{-1}))^{0.885} \quad (2)$$

to calculate the SFR from the $24\mu\text{m}$ luminosities obtained with Spitzer. We used this formula to estimate the SFR of the galaxies in our sample and display them as red points in Fig. 3. As we can see the $24\mu\text{m}$ estimates and those from the model fit to the whole SED, agree fairly well, having a ratio with a median value of unity and a standard deviation of 0.51dex . The scatter does not seem to correlate with the galaxy mass or luminosity. To examine whether the scatter is due to the absence of far-IR measurements, for a large fraction of the galaxies in our sample we selected 35 galaxies for which IRAS and Akari fluxes were available and fit them again with the model, removing this time the far-IR points. We then compared the new estimates of the

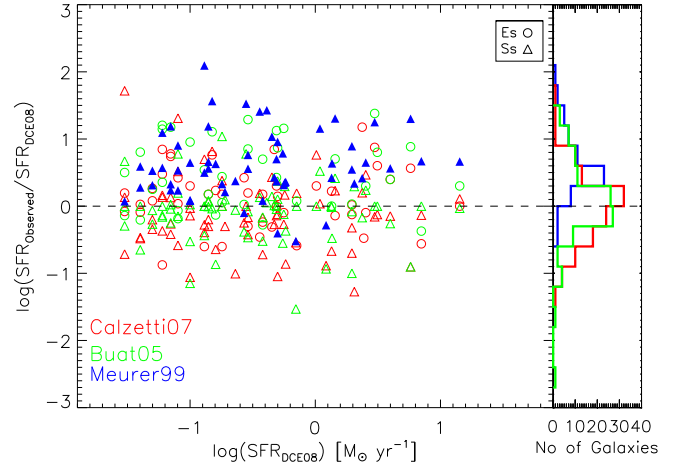


Fig. 3. A plot of the ratio of the SFRs derived from the observed FUV or $24\mu\text{m}$ fluxes over the SFRs derived from the da Cunha et al. (2008) model as a function of the model SFR. Red open circles and red open triangles are the SFRs derived from the MIPS $24\mu\text{m}$ fluxes for early and the late-type galaxies respectively. Green open circles and green open triangles mark the estimates based on the FUV to infrared excess as described by Buat et al. (2005). Filled blue triangles indicate late-type galaxies for which the SFRs are derived from the FUV after estimating the extinction using the β slope method of Meurer et al. (1999). The dashed line is the one-to-one relation. The histogram of the ratios for each method is indicated on the right panel.

SFRs with the ones when all data were used and found that they were very similar, their average ratio being 0.95 and the corresponding standard deviation 0.19 . A possible explanation for the scatter between the results of the model and the Calzetti et al. (2007) method could be related to variations in the metallicity of the galaxies (i.e. Rosenberg et al. 2008). Another factor which may influence the SFR values, related to the star formation history of the galaxies, is the fact that in the da Cunha et al. (2008) model the star formation rates are averaged over 100Myr , while the Calzetti et al. (2007) assumes a timescale of 10Myr .

In the UV the integrated spectrum is dominated by young stars, and so the SFR scales linearly with luminosity. However in order to use the UV to trace SFR, we have to correct the attenuated UV fluxes for dust extinction. One method to do this is to use the β -slope correction,

$$\beta(\text{GALEX}) = \frac{\log(f_{\text{FUV}}) - \log(f_{\text{NUV}})}{\log(\lambda_{\text{FUV}}) - \log(\lambda_{\text{NUV}})} \quad (3)$$

where f_{FUV} and f_{NUV} are the flux densities per unit wavelength in the FUV and NUV bands respectively, $\lambda_{\text{FUV}} = 1520\text{\AA}$, and $\lambda_{\text{NUV}} = 2310\text{\AA}$. Then we can apply the relation of Meurer et al. (1999) for starburst galaxies,

$$L_{\text{FUV,cor}} = 10^{0.4(4.43+1.99\beta)} L_{\text{FUV,obs}} \quad (4)$$

where L_{obs} and L_{cor} are the observed and extinction corrected FUV luminosities and finally we can derive the SFRs using the relation of Salim et al. (2007):

$$\text{SFR}_{\text{FUV}}(M_{\odot}\text{yr}^{-1}) = 6.84 \times 10^{-29} L_{\text{FUV,cor}} \quad (5)$$

for Chabrier IMF.

The SFRs of the early-type galaxies cannot be estimated using this method since the β -slope is mainly determined by the old stellar population rather than the dust extinction and thus their extinction corrected UV luminosities are completely overestimated. Even for late-type galaxies though, when we compare in Fig. 3 the FUV estimates of the SFR with the corresponding values obtained with the model we find that the former are overestimated by a factor of 0.56dex with a global scatter of 0.46dex. We attribute this to the calibration of the extinction correction of Meurer et al. (1999) who used a sample of local UV-selected starburst galaxies with high dust content, quite dissimilar to the HCG galaxies. As discussed in detail by Kong et al. (2004), this results in overestimating the UV corrected luminosities and consequently to an overestimate of the SFRs. Indeed, when we plot the FIR-to-UV luminosities of our galaxies against the spectral slope (β -slope) we notice that at a fixed β all the galaxies have systematically lower ratio of total to FIR-to-UV luminosities than the starburst galaxies of Meurer et al. (1999). On the other hand, galaxies HCG16c and HCG16d which are infrared luminous ($L_{\text{IR}} > 10^{11} L_{\odot}$), have SFRs which are very similar to those derived by the model (10.02 and $1.52 M_{\odot} \text{yr}^{-1}$ respectively).

Since, the previous method overestimates the SFR, we can also use the relation of Buat et al. (2005). These authors used the infrared to UV luminosity ratio to quantify the dust attenuation in the FUV band of GALEX for a wider sample consisted of more quiescent galaxies. The formula they derived to correct for dust extinction is described by the following relation:

$$A_{\text{FUV}} = 0.0333y^3 + 0.3522y^2 + 1.1960y + 0.4967 \quad (6)$$

where $y = \log(F_{\text{dust}}/F_{\text{FUV}})$ is the ratio of the infrared to FUV flux densities. To derive these ratios for our galaxies we used the infrared luminosities estimated by our SED modelling, as well the observed UV luminosities and estimated the SFR using the formula (4) of Iglesias-Páramo et al. (2006) :

$$\log[\text{SFR}_{\text{FUV}}(M_{\odot} \text{yr}^{-1})] = 0.63 \times (\log[L_{\text{FUV,corr}}(L_{\odot})] - 9.51) \quad (7)$$

where the $L_{\text{FUV,corr}}$ is the extinction corrected FUV luminosity (in L_{\odot}) and the factor of 0.63 has been introduced to correct for the Chabrier IMF (Chabrier 2003; da Cunha et al. 2008). The results are presented in Fig. 3 in green. We notice that the ratios of the SFRs are uniformly distributed around ~ 1.05 displaying a scatter of 0.56dex and also agree with the $24\mu\text{m}$ estimates. Given the success of the model in a variety of systems (see da Cunha et al. 2008; da Cunha et al. 2010a,b) we will base the remaining of the analysis in the model derived SFRs.

4. Results

4.1. Evolutionary state of the groups

In order to study the star formation properties of HCGs groups, Bitsakis et al. (2010) separated them into dynamically “young” and dynamically “old”. We classified a group as dynamically “young” if at least 75% of its galaxies are late-type. Conversely, a group is dynamically “old” if more than 25% of its galaxies are early-type. It is known that the specific star formation rate (sSFR), is a tracer of the star formation history of a galaxy, and galaxies in compact groups do experience multiple encounters with the various group members. Consequently, we would expect that a young group is more likely to have a larger fraction of late-type galaxies, since its members would not have enough time to experience multiple interactions which would trigger star formation, consume the available gas and transform them into

early-type systems. Furthermore, these late-type galaxies would have not built up much of their stellar mass. They would still have larger amounts of gas and dust, as well as higher SFRs and sSFR. On the other hand, if a group is dominated by early-type systems, it would be dynamically “old”, since interactions and possible merging of its members over its history would have led to the formation of some of those ellipticals. As a result, the spirals in these groups would have already built some of their stars and their sSFR would be lower. In our present sample, 10 groups (HCG2, 7, 16, 38, 44, 47, 54, 59, 91 & 100) are classified as dynamically “young” and the remaining 22 as dynamically “old” (see Table 7).

We notice that in the majority of the groups (80%) which are classified as dynamically “old”, the most massive galaxy that dominates is an early-type galaxy displaying a median stellar mass of $1.2 \times 10^{11} M_{\odot}$. In all dynamically “young” groups the dominant galaxy is a late-type, with a median stellar mass of $5.1 \times 10^{10} M_{\odot}$. These most massive galaxies of each group, are marked with a star in Table 4. Despite the fact that there are just 10 dynamically “young” groups in our sample and we could be affected by small number statistics, we note that dynamically “old” groups have on average 4.7 members in each, more than the “young” groups which only have 4 members.

A different classification of the HCGs into three phases, 1, 2, and 3, based on their HI gas content was proposed by Verdes-Montenegro et al. (2001). In the first phase the HI gas is mainly associated with the disks of galaxies. In the second, 40-70% of the HI is found in the disks of the galaxies and the rest has been stripped out, due to tidal stripping, into the intra-group medium. Finally, in the third phase are groups with almost all their HI located outside of member galaxies, or in a common envelope engulfing most group members. Using this classification Borthakur et al. (2010) classified 14 of the groups in our sample and the results are presented in Table 7. Both our, as well as Verdes-Montenegro et al. (2001) classification method, are based on how galaxy interactions and merging affect the morphology of the group members, thus they are related to their evolution. There is a global agreement between the two methods for 12 of the 14 groups we have in common. We will discuss these in more detail in Sect. 4.6.

4.2. The physical properties of HCG galaxies

We will now use the results of the SED modelling, described in the previous section, to examine the physical parameters of the galaxies in our sample and compare them with the ones derived for the comparison samples. The large number of galaxies, a total of 135 in 32 groups, is sufficient to produce statistically significant results in order to explore these parameters.

In panel a of Fig. 4 we present the distributions of the stellar masses separated in early- (E’s and S0’s) and late-type (S’s and Irr’s) galaxies in groups, marked in red and blue respectively. We can see that the distributions are not too different as a two-sided Kolmogorov-Smirnov (KS) suggests that the probability (P_{KS}) that the two samples are drawn from the different populations is ~ 0.04 . The median stellar masses of the late and early-type galaxies in our sample are $1.78^{+0.79}_{-0.55} \times 10^{10} M_{\odot}$ and $4.07^{+0.72}_{-0.60} \times 10^{10} M_{\odot}$ respectively. One might have expected that the late-type galaxies would have much lower stellar masses compared to the early-types since the latter had more time to increase their stellar mass as they converted their gas into star and/or resulted from the merging of late type systems. However, as we know tidal interactions play an important role

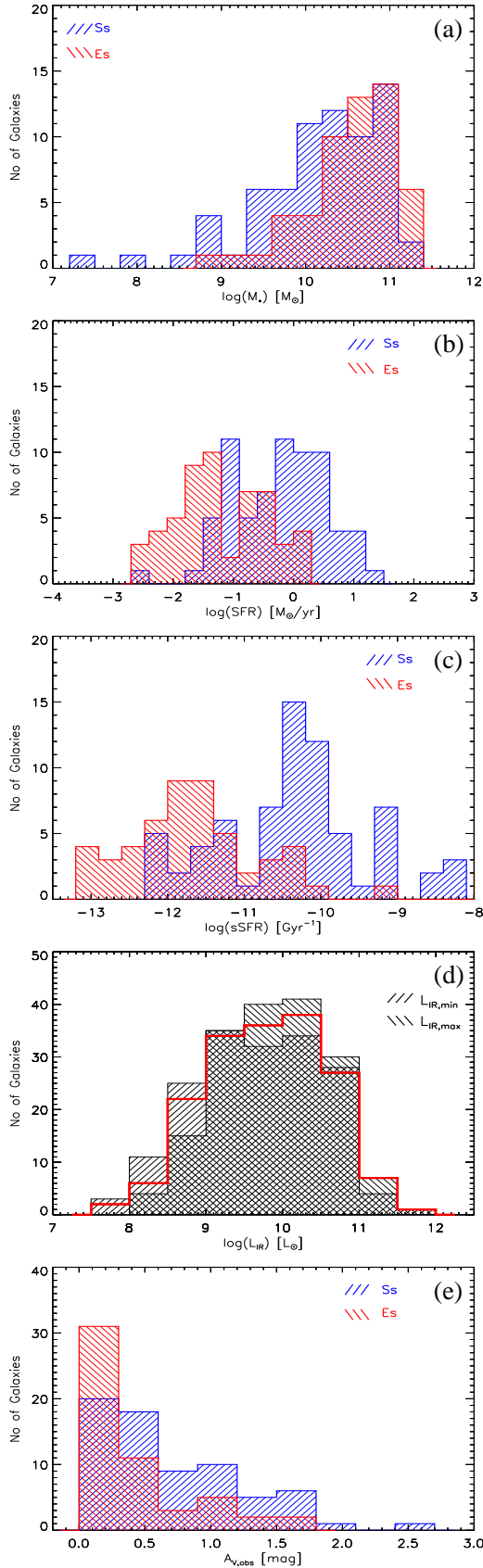


Fig. 4. Histograms of several properties of our HCG sample. Early type galaxies are marked in red and late type galaxies in blue a) the distributions of the stellar masses (M_*). b) the distributions of the star formation rates (SFR). c) the distributions of specific star formation rates (sSFR). d) The histogram of the infrared luminosities, L_{IR} , in red, as estimated by our SED modelling. Because of the absence of far-IR observations for most of the sample we overplot in hashed areas the histograms corresponding to the minimum and maximum L_{IR} of each galaxy, associated to the 16th and 84th percentile range of the best fit respectively. e) A histogram of the extinction inferred from the SED fit ($A_{V,\text{obs}}$) as measured model-derived attenuated and unattenuated SED (see Section 3.1.3).

in triggering star formation in galaxies (Struck 1999). Compact groups have high galaxy density, display signs of interaction (eg Verdes-Montenegro et al. 2001) and contain galaxies which are actively forming young stars. Furthermore, as we showed in the previous section, most of the massive late-type galaxies are found in dynamically “old” groups. We thus believe that several of the HCG late-type galaxies have already increased their stellar mass, due to past tidal encounters. We will examine more specifically these galaxies and their properties in the next section.

In Fig. 4b we present the distributions of the star formation rates of early and late-type galaxies in groups. As it was expected most of the late-type galaxies have higher SFRs than the early-type systems, their median SFR being $0.60^{+0.12}_{-0.14} M_\odot \text{yr}^{-1}$ compared to $0.05^{+0.02}_{-0.01} M_\odot \text{yr}^{-1}$. The maximum SFR seen in our sample is $\sim 26 M_\odot \text{yr}^{-1}$, typical of starbursts in the Luminous Infrared Galaxy (LIRG) range. We should note that there are 8 early-type galaxies with relatively high SFRs ($\sim 1-5 M_\odot \text{yr}^{-1}$) which is more than an order of magnitude higher than what is observed in the rest of the sample. We will discuss these galaxies in more detail in Section 4.4.

In panel c of Fig. 4 we display the distributions of the sSFRs of our sample. We can see that there are late-type galaxies with rather low sSFRs ($\sim 10^{-12} \text{yr}^{-1}$). These galaxies, which belong to dynamically “old” groups, must have had already increased their stellar masses, thus decreasing their sSFRs, as a consequence of dynamically triggered star formation events due to past interactions. On the other hand, there are early-type galaxies which display rather high sSFRs ($\sim 10^{-10} \text{yr}^{-1}$). One explanation is that accretion and merging of gas rich dwarf companions has increased the gas content of these galaxies and they are currently forming stars. However, it is also possible that these galaxies are misclassified, dust obscured, edge on late-type systems. In Sections 4.3 and 4.4 we examine in more detail the sSFR distribution as a function of the dynamical state of each group, study the mid-IR and optical colors of the galaxies and compare them with our control samples.

In Fig. 4d we present, in red, the distribution of the infrared luminosities (L_{IR}) as estimated from the da Cunha et al. (2008) model. Since no far-IR observations were available for most of the galaxies (74%) of our sample, the L_{IR} can not be robustly constrained. Using for each galaxy the minimum and the maximum values of the probability distribution functions as reported by the model, we create two additional histograms corresponding to the low and high values respectively. We observe that the overall shape and median value of the distribution does not change substantially. The median L_{IR} of the sample is $5.0^{+3.0}_{-0.9} \times 10^9 L_\odot$ and most of the HCG galaxies are not IR luminous ($L_{\text{IR}} \geq 10^{11} L_\odot$). There are only 7 galaxies, HCG4a, HCG16c, HCG16d, HCG38b, HCG91a, HCG92c and HCG95a, with $L_{\text{IR}} > 10^{11} L_\odot$. Note that these are all late-type systems, they are detected in the far-IR, and the first 5 are found in dynamically “young” groups.

As we discussed in Section 3.1.3 we can use the model-derived attenuated (observed) and unattenuated SEDs to estimate the V-band optical depth ($A_{V,\text{obs}}$) for each galaxy. Two histograms of these values, for the early and late-type systems, are presented in Fig. 4d. The median $A_{V,\text{obs}}$ is $0.23 \pm 0.17 \text{mag}$ and $0.58 \pm 0.36 \text{mag}$ for the early and late-type galaxies, respectively. We observe that there are 8 ($\sim 14\%$) of the early-type galaxies, with extinctions similar to what is seen in dusty late-type galaxies ($\geq 1 \text{mag}$). These are HCG4d, HCG55c, HCG56b, HCG56d, HCG56e, HCG71b, HCG79b, HCG100a. We should note that these galaxies are the ones forming the tail of early-type galax-

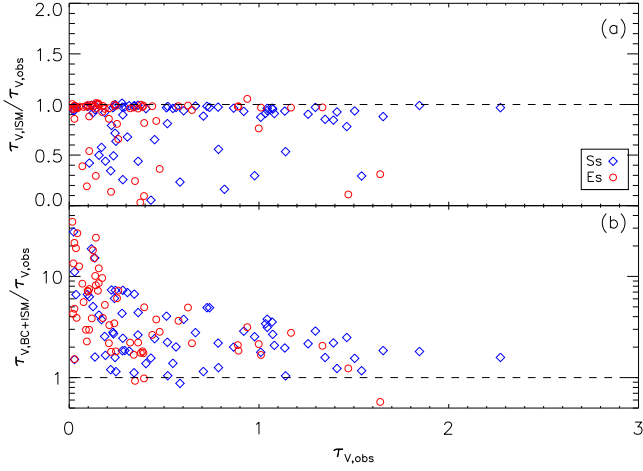


Fig. 5. a) Ratio of the intrinsic $\tau_{V,ISM}$ derived by the model over the observed (attenuated spectrum) $\tau_{V,obs}$ versus the $\tau_{V,obs}$. The dashed line is the one-to-one ratio. The red circles represent the early-type galaxies in HCGs and the blue diamonds the late-type ones. b) Ratio of the intrinsic τ_V for stars in birth clouds, derived by the model over the observed $\tau_{V,obs}$ versus the $\tau_{V,obs}$, using the same notation. We excluded from the plot 6 galaxies (HCG44a, HCG47a, HCG47b, HCG56b, HCG59a and HCG68a) since their χ^2 of model-fit was more than 9.00 and the derived τ fairly uncertain (See Table 3).

ies with high SFRs and sSFRs, mentioned above. The fact that they appear to have larger amounts of dust than what one may expect for early-type galaxies, as well as the fact that they display higher star formation activity, further supports the idea that these may indeed be misclassified late-type systems.

The model of da Cunha et al. (2008) also estimates the total effective V-band absorption optical depth of the dust seen by a young star ($\tau_V = \tau_{V,BC} + \tau_{V,ISM}$) inside the stellar birth clouds, and the fraction of the absorption (μ) contributed by dust found in the diffuse ISM along the line of sight. The emission from young stars is more attenuated than that from old stars. In young stars the extinction is dominated by the dust of the surrounding birth clouds with an additional component due to the dust in the diffuse ISM traversed by their light. Older stars ($> 100\text{Myr}$), which have dispersed their birth clouds, are only affected from the dust found in the diffuse ISM. Consequently, one would expect that in early-type galaxies, where currently no recent star formation is taking place, the optical light would be dominated by the old stars and therefore, the representative obscuration would be that of the ambient ISM. In late-type galaxies the total extinction would be the contribution of both components, BC and ISM. In that case, each component will contribute differently, depending on how much of the optical energy production in the galaxy is due to stars within the birth clouds. We would like to emphasize that since both components can contribute to a different extent at different wavelengths, the representative extinction of a galaxy varies also with wavelength, and that is why here we consider only optical light, instead of referring to the total energy output of the galaxy.

Using the output of the model, we can thus estimate the optical depth contributed from the diffuse ISM, $\tau_{V,ISM} = \mu \tau_V$, and the optical depth from the stellar birth clouds, $\tau_{V,BC} = (1 - \mu) \tau_V$. In Table 4 we present the optical depth derived from the attenuated and unattenuated SED, $\tau_{V,obs}$, the $\tau_{V,ISM}$, as well as the to-

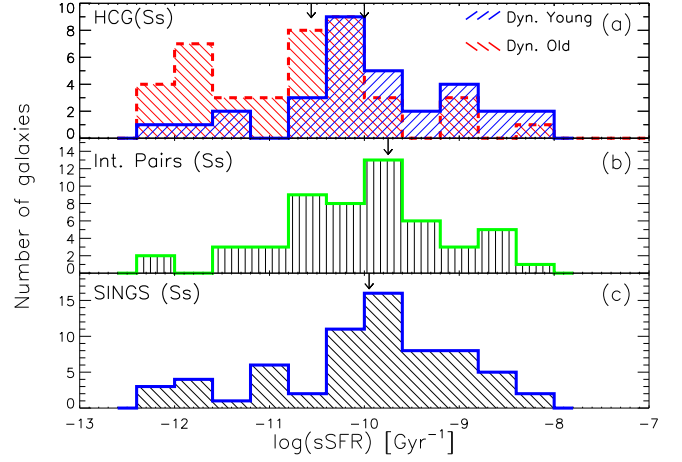


Fig. 6. Histograms of the specific star formation, sSFR, of the late-type galaxies our three samples, estimated by modelling their SED. The top plot displays in blue the histogram of the sSFR of the 31 late-type galaxies found in dynamically-young, spiral-dominated groups. Over-plotted in red is the corresponding histogram of the 42 galaxies in dynamically-old elliptically dominated groups. The middle and bottom plots present the histograms of the 52 late-type galaxies in the Smith et al. (2007a) interacting galaxy pairs, as well as the 71 SINGS late-type galaxies. The arrows indicate the median sSFR value of each distribution.

tal optical depth seen by young stars inside stellar birth clouds, $\tau_V = \tau_{V,BC} + \tau_{V,ISM}$. In Fig. 5, we plot the ratios of the intrinsic, model-derived optical depth (ISM and BC+ISM components) versus the observed optical depth, $\tau_{V,obs}$, we measured from the SED. We note that in most galaxies the ratio of $\tau_{V,ISM}$ over $\tau_{V,obs}$ is very close to unity. For these galaxies, in particularly for those with low extinction values, it is the dust in the ISM which determines the overall absorption of the emitted radiation. The contribution of the BC component is a small fraction of the overall light. On the other hand there are 28 galaxies with ratios lower than unity. From these, 18 are classified as late-type, half of them belong to dynamically “young” groups, and 10 are classified as early-type, 6 of which we believe are likely misclassified late-type systems (see Section 4.4 and Appendix). In the bottom panel of the same figure we plot the ratio of total τ_V over the $\tau_{V,obs}$, versus the $\tau_{V,obs}$. We notice that there are galaxies with very high τ_V over $\tau_{V,obs}$ values at small $\tau_{V,obs}$, most of which are early-type systems. Even though these galaxies have had recent ($< 100\text{Myr}$) star formation events, this does not dominate their global emission. We do note though, that as the $\tau_{V,obs}$ increase, the ratio converges towards unity, implying that the contribution of light from young stars in the BC component becomes a considerable fraction of the total emission, making the obscuration seen by the newly formed stars more representative of the observed obscuration of the galaxy.

4.3. HCG late-type galaxies

It has been well established that interactions can trigger star formation in galaxies (i.e. Struck 1999). During an interaction between two late type galaxies their atomic gas, typically found in diffuse clouds, collide. Shocks are produced which in turn increase the local gas density thus triggering bursts of star forma-

tion. The fact that the group environment has played an important role in the evolution of its member galaxies, is evident since the fraction of early-type systems in groups is higher than what is found in the field. So one would expect that because of their proximity, the late-type galaxies in groups would display different star formation properties from the ones in the field. However, in a preliminary analysis of 14 groups, Bitsakis et al. (2010) found that overall there is no evidence that the SFR and sSFR in late-type galaxies of HCG is different from galaxies in the field or in early-stage interacting systems. Interestingly though, when they separated their HCG sample into two sub-samples, namely the dynamically “old” and dynamically “young” groups (see Sect. 4.1 for the definition), late-type galaxies in dynamically “old” HCGs showed lower sSFRs than those in dynamically “young” groups. This was attributed to the likely larger number of past interactions experienced in the dynamically “old” groups, which would lead to a faster increase of their stellar mass compared to galaxies in young group. The higher stellar mass would reduce their current sSFR, even if subsequent gas accretion would result in star formation activity in them.

We re-examined this issue using our larger sample of 32 groups which contains 73 late-type galaxies and derived their sSFR as well as the one of the control samples, using the SED model of da Cunha et al. (2008). The results are shown in Fig. 6 and Table 3. Galaxies in dynamically “young” groups have a median sSFR of $8.51^{+4.07}_{-2.75} \times 10^{-11} \text{ yr}^{-1}$, while for galaxies in the dynamically “old” groups $\text{sSFR} = 2.75^{+2.03}_{-1.16} \times 10^{-11} \text{ yr}^{-1}$. Similarly, galaxies in interacting pairs have a $\text{sSFR} = 11.20^{+3.67}_{-2.70} \times 10^{-11} \text{ yr}^{-1}$ and in field galaxies $\text{sSFR} = 15.30^{+5.65}_{-4.29} \times 10^{-11} \text{ yr}^{-1}$. An analysis using two sided KS test indicates that there is no statistical difference between the samples of late-type galaxies in dynamically “young” HCGs and those of the SINGs and interacting pair samples ($P_{\text{KS}} > 0.80$). However, the same KS test reveals that the late-type galaxies in dynamically “old” groups, having a median sSFR which is more than three times lower, can not be drawn from same parent distribution as the other three samples ($P_{\text{KS}} \sim 10^{-3}$). Investigating in more detail the reason for this disparity, we find that it cannot be attributed to depressed SFR but instead it is due to a substantially more massive stellar content ($\sim 3 \times 10^{10} M_{\odot}$), similar to what is found early-type systems. This confirms the results and interpretation of Bitsakis et al. (2010) who relied on semi-empirical estimates of the sSFR on a smaller galaxy sample. Based on those findings one would also expect that due to their higher stellar mass, the late-type type galaxies in dynamically “old” groups should have redder UV and optical colors than late-type galaxies in the field. We examine this in Section 4.5.

4.4. HCG early-type galaxies

We showed in the previous section that the group environment affects the star formation history of the late-type members increasing their stellar mass in the process of transforming them into early-type systems. However, is there any evidence indicating that the early-type galaxies in groups are distinctly different from similar galaxies found in the field? Based on our SED modelling, we have already showed in Fig. 4, that nearly 15% of all early-type galaxies have SFRs and dust extinction similar to what is seen in late-type systems. We suggested that there are two possible explanations for this. One was that they were simply misclassified as Es or S0s, while in fact they are edge-on late-type systems. The second was that these galaxies even if they are early-type, based on their optical morphology, they

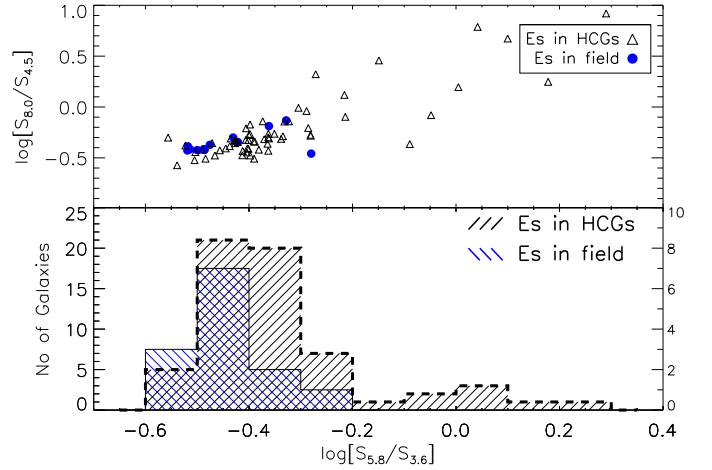


Fig. 7. Top panel: IRAC color-color plot of the early-type galaxies in HCGs (black open triangles) and a sample of field ellipticals (blue filled circles). Bottom panel: The histograms of the $\log[S_{5.8}/S_{3.6}]$ color of the two samples. The early-type galaxies in the groups are marked with a black line (left axis) while the field ellipticals are presented in blue (right axis).

have experienced minor merging with gas/dust rich dwarf companions in the groups, which has increased their gas content, star formation activity, and dust extinction.

According to Hickson (1982) the classification of the HCG galaxies was performed using their morphological features, optical colors, and sharpness of the edge of the image. For all groups of our sample though, we also have Spitzer mid-IR images which provide additional information on their properties. It is well known that the mid-IR spectra of the star forming galaxies in addition, to continuum emission due to warm dust, are also filled with a series of broad emission features between 3 to $18 \mu\text{m}$, which can contribute up to 20% of their total IR luminosity (Dale et al. 2005; Smith et al. 2007b). These features are the vibrational modes of Polycyclic Aromatic Hydrocarbons (PAHs), which absorb UV photons from newly born stars and re-emit them in the mid-IR. Typically only late-type galaxies with active star formation and dust emit strongly in these bands. Some PAHs have also been detected in some early-type systems, but they display peculiar PAH-band ratios (Bressan et al. 2006; Kaneda et al. 2008; Panuzzo et al. 2011). To probe the properties of the early-type galaxies in the groups, we examine their mid-IR colors and compare them with isolated ellipticals in the field which are not expected to have PAH emission. In Fig. 7 we use our Spitzer/IRAC photometry and plot the 8.0 to $4.5 \mu\text{m}$ flux density ratio as a function of the 5.8 to $3.5 \mu\text{m}$ ratio for the early-type galaxies of our HCG sample, as well as the control sample of field ellipticals. Weak PAHs would result in low values of both ratios since the 6.2 and $7.7 \mu\text{m}$ features, which contribute $\sim 50\%$ of the total PAH emission, are sampled by the 5.8 and $8.0 \mu\text{m}$ IRAC filters (Smith et al. 2007b). Indeed, we observe that most of the early-type galaxies in groups, as well as in the field are concentrated in the lower left part of the color-color plot of Fig. 7. These galaxies are very close to the $(-0.4, -0.5)$ locus of pure stellar photospheric emission where the flux density in the mid-IR scales with λ^{-2} . Consequently, they are expected to have very weak dust and PAH emission. On the other hand, the upper right quadrant of the figure should be populated by galaxies with strong PAH features

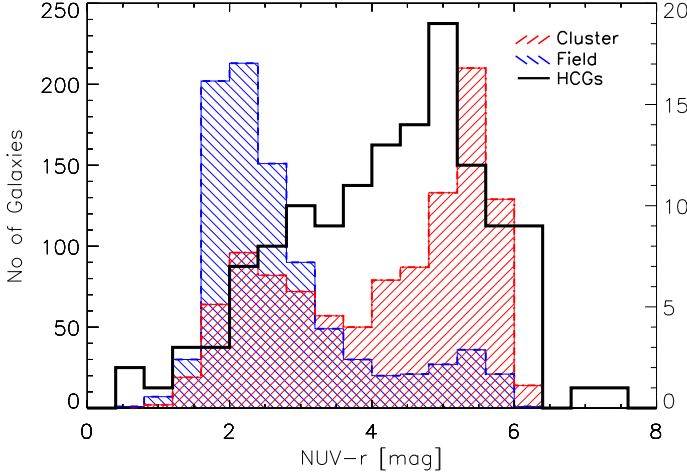


Fig. 8. NUV-r histogram of our HCG galaxy sample shown in black (right Y-axis). The histograms of the of field, in blue, and cluster galaxies, in red, from the Haines et al. (2008) control sample are also presented (left Y-axis).

and possibly some hot dust contribution, as a result of intense star formation and/or AGN activity. As expected, no field ellipticals are seen in this quadrant. However, there is a “tail” of 10 early-type HCG galaxies ($\sim 16\%$ of the total) extending to this part of the plot (for $\log[f_{5.8}/f_{3.6}] > -0.25$). Examining the 5.8 to $3.5\mu\text{m}$ IRAC color distributions of HCG and field with a KS test, we find that they are different ($P_{\text{KS}} \sim 0.005$). The early-type galaxies with red IRAC colors are: HCG4d, HCG40f, HCG55c, HCG56b, HCG56d, HCG56e, HCG68a, HCG71b, HCG79b & HCG100a. We note that HCG40f and HCG68a are at the left edge of the color selection and it is possible that contamination from a red nearby companion is affecting their mid-IR fluxes. All these galaxies are examined in more detail in the Appendix, where we display their SEDs, Ks-band contour plots and “true color” composites based on their Spitzer/IRAC mid-IR images. Based on this analysis and previous suggestions, we propose that 7 of them, HCG4d, HCG55c, HCG56d, HCG56e, HCG71b, HCG79b & HCG100a are likely dust obscured late type systems. Furthermore, if HCGd and HCG71b are indeed late-type galaxies, then their groups must be reclassified as dynamically “young” (instead of “old”). In the remaining of the paper we will consider them as such (see Table 6 and Table A.1).

4.5. Bimodality in HCG galaxy colors

In the previous sections we have examined several of the physical parameters of our HCG sample as derived by the SED modelling. In order to examine more thoroughly the evidence of evolution due to the group environment, we will now compare all our results based on the UV, optical, and infrared imaging as well as the available spectroscopic diagnostics.

A number of studies of galaxies have revealed a bimodality in the UV-optical colors of galaxies in field and in clusters (e.g. Wyder et al. 2007; Haines et al. 2008). This type of bimodality in the colors of the late- and early-type galaxies is real and directly connected to the original galaxy classification scheme by Hubble. It appears quite strongly in the NUV-r color distribution of a sample and consists of two peaks, called the “red sequence” and the “blue cloud”, and a minimum in between them identified as the “green valley” (see Strateva et al. 2001).

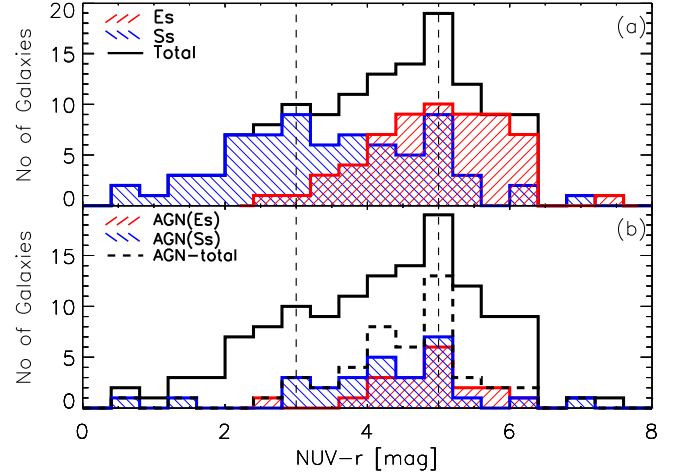


Fig. 9. a) NUV-r histogram of the whole HCG galaxy sample is shown in black. The corresponding histograms of the early- and late-type galaxies of the sample, classified according to their optical morphology, are shown with the red and blue shaded areas. b) The NUV-r distribution of the galaxies hosting an AGN is indicated with the dashed dark line. As above, the early- and late-type hosts are indicated with the red and blue histograms. The region of $3 < \text{NUV-r} < 5$, identified as “green valley”, is marked with the vertical dashed lines.

Wyder et al. (2007) examined a sample of over 18,000 galaxies observed with GALEX and SDSS and showed that a NUV-r versus M_r color magnitude diagram can be used to separate them into (i) passively evolving, (ii) star-forming and (iii) AGN components. Passively evolving galaxies are well confined to the “red sequence” ($\text{NUV-r} > 5$), with few showing blue UV-optical colors, while all blue galaxies, with $\text{NUV-r} < 3$, are spectroscopically classified as star forming (see also Haines et al. 2008). AGN seem to dominate the area of the green valley” ($3 < \text{NUV-r} < 5$). The small fraction of galaxies in the “green valley” can be understood from the fact that galaxies do not spend so much time at these colors. Using Starburst99 (see Leitherer et al. 1999) we simulated the evolution of a stellar population typical of a spiral galaxy assuming solar metallicity and either a continuous star formation (of $1\text{M}_{\odot}\text{yr}^{-1}$) or a single starburst (producing total stellar mass of 10^6M_{\odot}). Depending on the assumptions, we find that the colors of the population place it within the “blue cloud” just for $\sim 5\text{--}7\text{Myr}$ and after spending only $\sim 1\text{--}5\text{Myr}$ transiting through the “green valley” it remains in the “red sequence” for the rest of its lifetime. Thus this color bimodality emerges from the nature of the galaxies as they evolve through time.

In Fig. 8 we plot the NUV-r colors of our HCG sample, as a black solid line, and compare them with the field and cluster galaxies of the Haines et al. (2008) sample, indicated in blue and red respectively. The three regions of the color space discussed by Wyder et al. (2007) are clearly visible. On the left, near $\text{NUV-r} \sim 2$, we identify the “blue cloud” where the field galaxy distribution peaks. Nearly 58% of the total number of field galaxies is found within 0.5mags of this color. Few of the galaxies in clusters (15%) are also seen in this area. To the right, near $\text{NUV-r} \sim 5.5$, we observe the “red sequence” where most (51%) of the cluster galaxies are concentrated. Only 16% of the field galaxies are found in the “red sequence”. The “green valley” is between the two peaks and is mostly (34%) populated by cluster galaxies (Haines et al. 2008). When we examine the

HCG NUV-r color distribution, we note a clear difference. Only 17% of their galaxies are in the “blue cloud”, a fraction similar to what is found for galaxies in clusters. However, the majority (73%) of the HCG galaxies are concentrated in the “green valley” and “red sequence” areas. A likely explanation would be that most of the HCG galaxies are already passively evolving or they are in the process of moving from the star-forming region to the “red sequence”. This is consistent with the fact that compact groups have a higher fraction of elliptical galaxies than the field. Another possibility is that some of these galaxies are in fact late-type systems which have redder colors and hence move to the right on the plot, because of dust extinction and/or due to the presence of a substantial older stellar population (post starburst galaxies). This is expected from our earlier findings regarding the miss-classification of a fraction of the early-type galaxies in the HCG and the lower sSRF in dynamically “old” groups.

To study in more detail how the NUV-r color distribution of the HCG galaxies is affected by their morphology and nuclear activity, we present in Fig. 9 the corresponding histograms based on their optical morphologies, as well as their nuclear spectral classification. We note that only 36% of the late-type galaxies, indicated in blue, are found within the “blue cloud”. However the majority of the HCG galaxies, almost 60%, are located in the “green valley” and in the “red sequence” ($\sim 13\%$). In Fig. 9b we present the same plot as at the top, but only for the galaxies of our sample who have an optically identified AGN. The whole distribution is shown with the black dashed line, while the distributions of early- and late-type AGN hosts are shown in red and blue. We performed a two sided KS test between the distribution of galaxies hosting an AGN and the total distribution of the HCG galaxies and we conclude that there is no statistical difference in their NUV-r colors ($P_{KS} \sim 0.25$). This suggests that the presence of an AGN does not affect substantially the UV-optical color of the galaxies in Hickson Compact Groups.

As we described earlier, more than 40% of the galaxies in our sample host an AGN into their nucleus. This, in addition with the fact that the code of da Cunha et al. (2008) does not include the contribution of an AGN to the SED of a galaxy, could bias some of our results, in particular the SFR, sSFR and the L_{IR} . Using the IRAC color-color AGN diagnostics introduced by Stern et al. (2005) we investigated the influence of the AGN to the mid-IR SED of the galaxies in our sample. Only three systems, HCG6b, HCG56b and HCG92c, have mid-IR SEDs which are consistent with a strong power-law continuum emission indicative of a strong AGN in their nucleus. For all remaining galaxies the optically identified AGN does not dominate their SED and thus their physical parameters estimated by our model are considered reliable.

In order to explore the color variations as a function of the evolution state of the groups, we plot in Fig. 10 the histograms of the early- and late-type galaxies found in the dynamically “young” and “old” groups respectively. Observing the top panel we find that almost 60% of the late-type galaxies in dynamically “young” groups are located within the “blue cloud” and 43% of them, for which nuclear spectra were available, host an AGN in their nucleus. There are also three outlier galaxies (HCG16b, HCG44a and HCG59a) which have red NUV-r colors ($>5\text{mag}$). It is possible, that these systems have built up their stellar mass in the past and their UV/optical colors are currently dominated by emission from old stars. In addition, past tidal interactions probably stripped some of their gas in the intragroup medium decreasing the fuel necessary for current star formation. In dynamically “old” groups the late-type galaxies are redder and as we can see in Fig. 10b most of them ($>63\%$) are located within

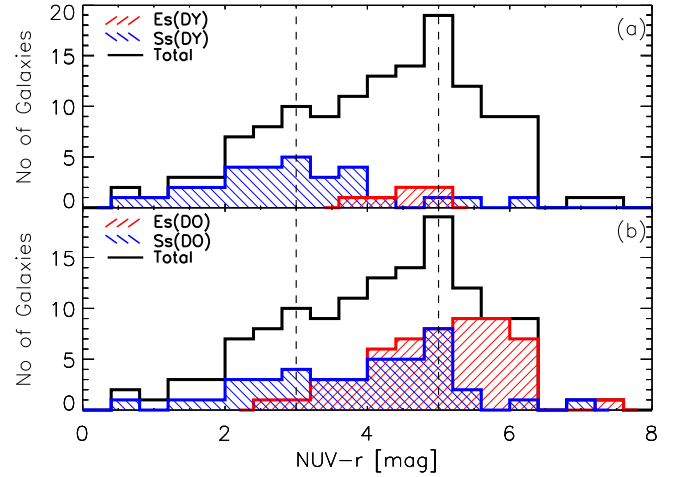


Fig. 10. a) NUV-r histogram of our HCG galaxy sample shown in black solid line. The corresponding histograms of the early- and late-type galaxies found in dynamically “young” groups are shown with the red and blue shaded areas respectively. b) Same as in a), but for the galaxies in dynamically “old” groups. The region of $3 < \text{NUV-r} < 5$, identified as “green valley”, is marked with the vertical dashed lines.

the “green valley”. As in dynamically “young” groups there are also four galaxies (HCG22b, HCG40d, HCG68c and HCG71a) in these groups which are found in the “red sequence”.

Overall 45% of the early-type galaxies, shown in red in Fig. 9, are located within the “red sequence” and the rest are along the “green valley”. As we mentioned earlier, these systems are expected to be passively evolving and thus, their colors should be dominated by old stellar populations. We find that this is the case for most of them, as only two are found in the “blue cloud”. We believe that these galaxies are misclassified late-type galaxies (see Sect. 4.4) and we examine them in more detail in the Appendix. From Fig. 10a we see that all early-type galaxies in the dynamically “young” groups are in the “green valley”. One could suggest that they were already early-type before reaching the group and the interactions and/or merging of dwarf companions in the group environment triggered the star formation activity and provide extra gas. However, the most possible explanation is that these are group galaxies which are currently migrating from the “blue cloud” to the “red sequence”. In that case, the morphological transformation should accompany the color transformation. Indeed, the galaxies located in bluer colors (around $\text{NUV-r} \sim 4$) are lenticulars, while the ones at $\text{NUV-r} \sim 5$ are ellipticals. Similarly, at the bottom panel of Fig. 10 we see that more than half of the early-type galaxies in dynamically “old” groups are located within the “green valley”. These galaxies are mostly ($>70\%$) S0/SB0’s. However, there is a large fraction ($\sim 25\%$) of elliptical galaxies which also have the same colors. We suggest that even though the morphology of a galaxy typically determines its colors, there are several of the group ellipticals which move back to bluer colors due to interactions and/or merging in the compact group environment.

As discussed before, we know that the UV-optical colors of a galaxy, are not only affected by its star formation history, but also from dust extinction. Thus, it would be useful to understand how much of the observed variation in colors is due to intrinsic extinction in the galaxies. Especially for the late-type galaxies which are located within the “green valley”, we have

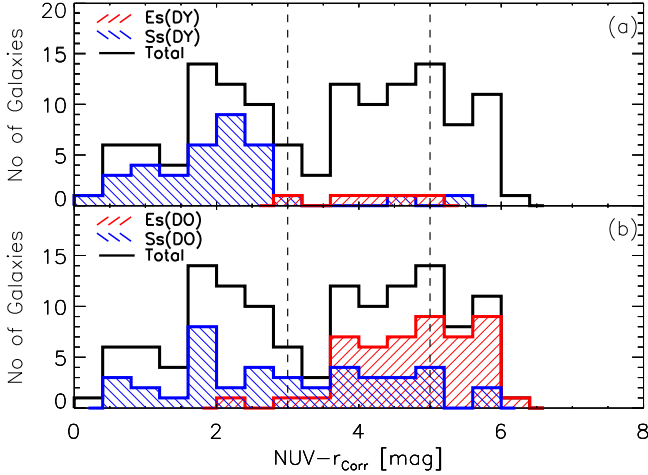


Fig. 11. A histogram of the NUV-r colors of the HCG sample after correcting for dust extinction, in shown with the black solid line. The separation in two panels for “young” and “old” groups as well as the symbols follow the notation of Fig. 10

to examine if their colors are affected more from dust or because they contain a substantial old stellar population. Our SED model allow us to estimate and correct for dust attenuation, thus we plot in Fig. 11 the distributions of the corrected NUV-r colors of the early- and late-type galaxies in dynamically “young” (top panel) and dynamically “old” groups (bottom panel). We notice in panel a that almost all late-type galaxies in “young” groups move back to the “blue cloud”, suggesting that it is the dust which plays a dominant role in their apparent colors. On the other hand, 40% of the late-type galaxies in dynamically “old” groups still remain in the “green valley” after the extinction correction. It seems that in those it is the old red stars that dominate their UV/optical colors. This also agrees with the results of Section 4.3 where these galaxies display low sSFRs. Moreover, one can notice the large fraction of early-type galaxies which after the extinction correction move to the “green valley” ($\sim 50\%$ of the galaxies at these colors). These galaxies display high sSFRs ($\sim 0.21 \times 10^{-11} \text{yr}^{-1}$), so their bluer colors are possibly due higher levels of current star formation. We should note that even though for most galaxies the observed optical extinction derived from the SED model (A_V) is not very high (see Fig. 4e and Table 3), due to the steepness of the extinction curve this translates to over 2mags of correction in the NUV.

Since dust appears to affect the UV colors of HCG galaxies, one could suggest the use of their mid-IR colors, because they trace the light which was originally absorbed by the dust grains in the UV-optical. In Fig. 12 we present the IRAC color-color diagram, also shown in Bitsakis et al. (2010), using our new, larger sample. The physical meaning of this plot was described extensively in Fig. 7. We notice that most of the late-type galaxies are located in the upper right quadrant of the plot, while most of the early-types are in the lower left. The 10 early-type galaxies which display red mid-IR colors are the ones we mentioned in Section 4.3. We observe that between the colors $-0.1 < \log[f_{8.0}/f_{4.5}] < 0.3$ and $-0.25 < \log[f_{5.8}/f_{3.6}] < -0.10$ there is a lower density of galaxies. Johnson et al. (2007) and Tzanavaris et al. (2010) proposed that this “gap” is related to an accelerated migration of the galaxies from star forming to quiescent. When we compare this result to Fig. 11 we notice that the galaxies in the upper right quadrant of the IRAC color-color plot

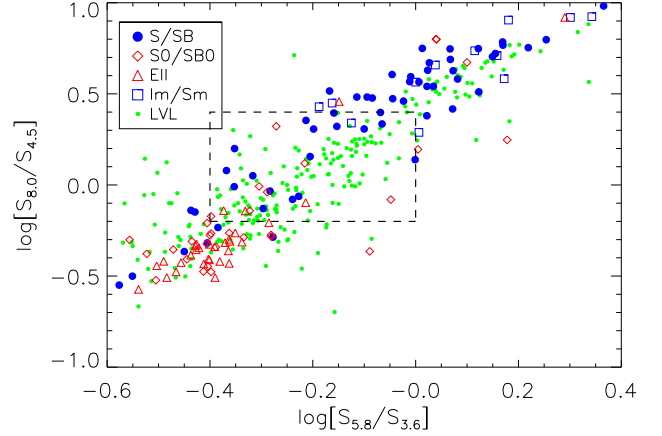


Fig. 12. The IRAC color-colors plot, originally presented in Fig. 7. Blue circles indicate the spiral galaxies of our HCG sample, blue squares are the irregulars, red triangles are the elliptical galaxies and red diamonds are the lenticular ones. Green dots indicate the LVL galaxies. According to Johnson et al. (2007) the “gap” is located in the area enclosed by the dashed lines.

are the ones with $\text{NUV-r} < 2.5$, while galaxies which are located in the lower left portion of the figure have $\text{NUV-r} > 3.5$. We finally notice that the lower galaxy density area appears in both figures and actually separates the star forming (“blue cloud”) from the passive evolving (“green valley” and “red sequence”) galaxies. Therefore we suggest that the color bimodality observed in the extinction corrected UV-optical colors, is also observed in the mid-IR and possibly emerges from the same physical properties of the galaxies.

How significant though is this “gap”? Walker et al. (2010) compared their sample of 12 HCGs with several control samples including the SINGS and interacting pair sample we used, as well as galaxies from the Coma cluster, and the Local Legacy Volume sample (LVL Dale et al. 2009). They concluded that the mid-IR color distribution of HCG galaxies is not seen in the field but it is seen in galaxies of the Coma infall region. However, in their analysis they combined the SINGS and LVL galaxies as a single local galaxy sample. As we mentioned though in Section 2.6.1, the SINGS sample was selected to explore the mid-IR properties of various galaxy types seen in the local universe, but it is not representative of a flux or volume limited population (Kennicutt et al. 2003). This selection biases the statistics of the colors of the sample. In contrast the LVL sample is volume limited, since it contains all known galaxies inside a sub-volume of 3.5 Mpc and an unbiased sample of spiral and irregular galaxies within the larger, more representative, 11 Mpc volume. The mid-IR colors of the LVL sample are plotted in Fig. 12 as green points. Performing a two sided KS-test between the distributions of the IRAC colors ($\log[f_{8.0}/f_{4.5}]$ and $\log[f_{5.8}/f_{3.6}]$) of HCG and LVL samples, we find that the distributions are not significantly different displaying $P_{KS} = 0.035$ and $P_{KS} = 0.028$, respectively. This suggests that there is no strong evidence that an accelerated evolution of galaxies in HCG is responsible for a significant fast change in their global mid-IR colors.

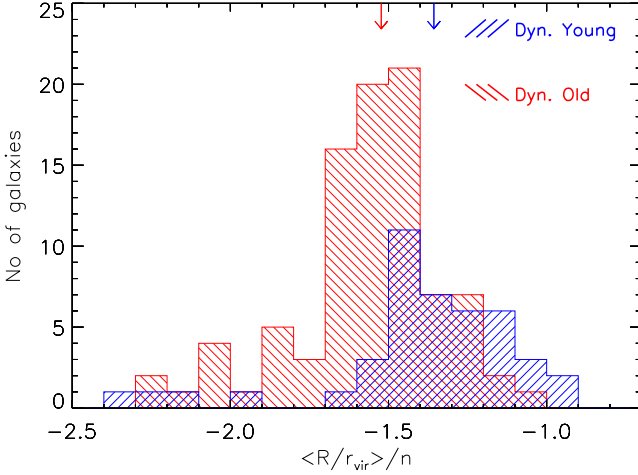


Fig. 13. Histograms of the “strength” of the dynamical interaction felt by each group galaxy ($\langle R/r_{\text{vir},\text{nei}} \rangle/n$). As usual, we separate our sample into dynamically “young” (blue) and dynamically “old” (red) groups. The arrows indicate the median values of the two distributions.

4.6. Dynamical properties of HCG galaxies

As we mentioned in Sect. 4.1 we classified the dynamical state of our sample depending on the fraction of elliptical galaxies they contain. Our method is related to their evolution since it is known that galaxy interactions and merging, transform galaxies from late-type systems to ellipticals. Thus, groups with excess of early-type members, are likely to be older and more compact. In order to investigate this we have estimated the projected distance of each galaxy from the other members of the same group members, as well as the virial radius of each galaxy. To calculate the projected distance between the group members we used the great circle distance relation. Then, using the relation described in Park & Hwang (2009), we estimated the virial radius with the formula:

$$r_{\text{vir}}(\text{Mpc}) = \left(\frac{3\gamma L \Omega_m}{800\pi\rho_m} \right)^{1/3} \quad (8)$$

where $L=10^{-0.4(M_r+20.00)}$ is the r-band luminosity in L_\odot and M_r is the absolute r-band magnitude of the galaxy, γ is the mass to light ratio (1 or 2 for late- and early-type galaxies, respectively), and $\rho_m=0.0223h^3\text{Mpc}^{-3}$ is the mean density of the universe, with $h=0.72$ and $\Omega_m=0.27$. Keeping in mind that compact groups may not be fully virialized dynamical systems, we present our results in Table 6. We note that indeed, in dynamically “old” groups the member galaxies are statistically closer to their nearest neighbors, having a mean projected distance of 26kpc compared to 37kpc for the dynamically “young” groups.

However, galaxies in groups are interacting not only with their nearest neighbors, but also with all other group members since in all cases the virial radii of the galaxies are substantially larger than the linear size of their group (see Table 6). To better quantify this effect we have followed the approach of Hwang et al. (2010), introducing the parameter of the “strength” of the interaction ($\langle R/r_{\text{vir},\text{nei}} \rangle/n$). This is estimated by averaging the ratios of the projected distances over the virial radii for all the neighbors of each galaxy and divide them by the total number of neighbors (n). This quantity provides an empirical measure of the interaction strength each galaxy experiences from its

companions. The smaller this parameter is, the stronger the dynamical influence of the companions.

In Fig. 13, we plot the distributions of the strengths according to the dynamical state of each group. Since we have SDSS data for only 74 galaxies and equation (6) relies on the SDSS r-band magnitude to compute the virial radius, we used the SED model fits to estimate the synthetic r-band magnitudes for the remaining of the sample. We observe that the “strength” parameter of dynamically “old” groups is indeed smaller than in dynamically “young” groups, suggesting that in the former the gravitational effects are stronger. A KS test between the two distributions confirms that the two distributions are significantly different ($P_{\text{KS}} \sim 10^{-5}$). Moreover, if we compare our results with the findings of Hwang et al. (2010) we see that the distances between the galaxies in groups and those of the centers of rich clusters are similar (both have $R < 0.5r_{\text{vir}}$). We can also estimate the velocity dispersion, σ_r , of each galaxy from the most massive-central galaxy of its group, using the published velocities from Hickson et al. 1992. Galaxies in dynamically “old” groups display mean velocity dispersion of $408 \pm 50 \text{ km s}^{-1}$, which is the half of what is observed in the Virgo cluster, in contrast with those in dynamically “young” groups for which is about $132 \pm 39 \text{ km s}^{-1}$. All these facts lead us to the conclusion that dynamically “old” groups, as their name implies, are older, denser and more evolved systems, since their properties are intermediate between those of rich clusters and dynamically “young” groups.

To further examine the dynamical properties of these groups, we can calculate their dynamical masses using the projected mass estimator from Bahcall & Tremaine (1981):

$$M_{\text{dyn}} = \frac{24}{\pi G N} \sum_{i=1}^N u_i^2 R_i, \quad (9)$$

where u_i is the difference in the recessional velocity between the group member i and the central massive object (see Table 4 where the most massive objects in each group are marked with a star), R_i is the projected distance from the central object, and N is the number of group members. This dynamical mass can be compared to the various components of the baryonic mass of the groups. The stellar mass is derived from our SED modelling while the total atomic hydrogen mass, M_{HI} , is available for 29 of the groups from Verdes-Montenegro et al. (2001). Unfortunately, the mass of the molecular hydrogen, M_{H_2} , is only available for 12 groups (Martinez-Badenes et al. 2011). We note that even though the integrated masses of the molecular and atomic hydrogen of the groups are often similar, on average they are both ~ 25 times less massive than the stellar component. These results are summarized in Table 7.

In Fig. 14 we separate our 32 groups in the two subsamples of dynamically “young” and “old” groups and present the corresponding histograms of the distributions of their atomic hydrogen, stellar, and dynamical masses.

We observe that the stellar mass distribution of dynamically “old” groups, shown in Fig. 14b is markedly different from that of dynamically “young” groups. A KS test confirms this, as the probability that the two are drawn from the same parent distribution is $P_{\text{KS}} \sim 0.009$. The median stellar mass of the dynamically “old” groups is $\sim 1.95 \times 10^{11} M_\odot$, more than double of what is seen in the “young” group subsample ($\sim 8.90 \times 10^{10} M_\odot$). This is understood on the basis of our classification scheme; dynamically “old” groups do have more elliptical galaxies which are typically more massive than spirals. Furthermore, from the anal-

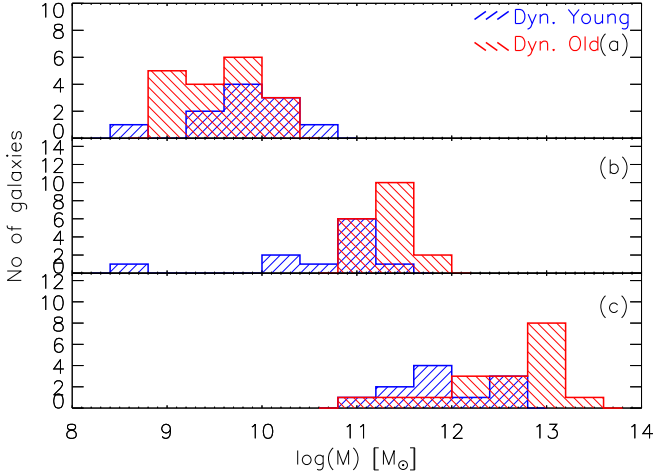


Fig. 14. a) Distributions of the total HI masses in the dynamically “young” (in blue) and the dynamically “old” (in red) groups, of the total stellar masses (panel b) and the total dynamical masses (panel c).

ysis of Section 4.3, we have shown that the late-type galaxies of these groups also have redder optical colors.

Surprisingly though, in Fig. 14a we note that the HI mass distribution is fairly similar in both subsamples ($P_{KS} \sim 0.26$), with a median value of HI mass $\sim 3.2 \times 10^9 M_\odot$. Assuming that dynamically “old” groups are older structures, with more early-type members which have already converted during a merging process a fraction of their gas into stars, it is not clear if what we see is a real “conspiracy” given the difference in star formation properties and relative amount of old stellar populations of the two subsamples. We know that a fraction of the HI gas is expelled from the galaxies to the intragroup medium in the form of plumes and long filaments as a group evolves progressively transforming the morphology of its members from late- to early-type (Verdes-Montenegro et al. 2001). However, the lifetime of these structures before they either change phase, as they interact with the hot intragroup gas, or are accreted back to the group members is not well constrained, since only a dozen of HCGs have high spatial resolution maps of their gas component.

Examining the distributions of the dynamical masses of the two subsamples in panel c of the same figure, we find that, as was the case with the stellar mass, these are also different ($P_{KS} \sim 0.008$). The dynamically “old” groups display a median dynamical mass of $6.46 \times 10^{12} M_\odot$, nearly an order of magnitude higher from what is seen in the “young” ones ($4.77 \times 10^{11} M_\odot$). Note, that the dynamical masses do not simply scale with the stellar mass of the subsamples, which only differ by a factor of ~ 2 . Furthermore, there is no indication of a variation in the ratio between the dark matter, as probed by the kinematics, and the baryonic matter in groups, or that there is a systematic error in the estimates of the dynamical mass due to one subsample being less virialized than the other. As a result, one could attribute the deficit in the observed baryons in the dynamically “old”, to a component of hot intragroup gas, since there is clear evidence that groups with more early type systems have stronger X-ray emission (Ponman et al. 1996; Mulchaey et al. 2003).

In Table 7 we also present our classification of the 32 groups, based on the fraction of the early-type members, as well as the classification based on their HI morphology proposed by Verdes-Montenegro et al. (2001) for 13 groups where this was

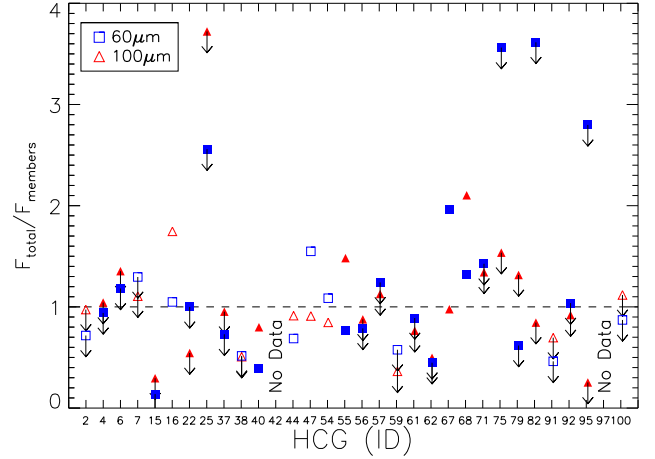


Fig. 15. Plot of the ratio of the observed IRAS 60 and 100 μm fluxes of each group divided by the corresponding flux all group members as predicted by our model fits. Since IRAS did not resolve/detect all the members of each group, several of the ratios are indicated as upper limits. Filled symbols indicate dynamically “old” groups.

available. Despite the small number statistics, we note that there is an overall agreement. Groups which we consider as dynamically old are in Phase 3 or 2 according to their HI content, while groups which we consider dynamically “young” are in Phase 1 or 2. There are two exceptions in this. HCG79, the so called “Seyferts’ Sextet” was classified by us as dynamically “old” but it is Phase 1 based on the distribution of its HI gas by (Borthakur et al. 2010). Inspecting it closely we see that our definition is likely marginal as the system does not have an elliptical galaxy and its 2 early type members are peculiar S0s. The other case is HCG44, which was classified as Phase 3 by Borthakur et al. (2010). The group consists of 3 late type galaxies and NGC 3193, an E2 which Aguerri et al. (2006) argue that may be an interloper. Close inspection of the HI map of the group shown in Fig. 2 of (Williams et al. 1991) reveals that nearly all gas emission is associated with the 3 late type systems, and only a small fraction is seen outside the galaxy disks. We would thus argue that this system is more likely in Phase 1 or 2, which would be consistent with our classification as dynamically “young”. Therefore, as expected, a change in the galaxy morphology also carries a change in the distribution of the atomic hydrogen within the group, and viceversa.

4.7. Diffuse Cold Dust in the Intragroup Medium

We mentioned earlier that using the model of da Cunha et al. (2008) we were able to derive several of the physical properties of the galaxies in our sample. Even though a number of parameters such as stellar mass and SFR, can be estimated with good accuracy, the lack of deep high spatial resolution wide field far-IR imaging, makes it very challenging to constrain the L_{IR} and accurately estimate the amount of cold dust in each galaxy.

As it was described in Bitsakis et al. (2010), there are several reasons to expect that the interactions among group members have expelled diffuse cold dust along with atomic gas in the intragroup medium. In this preliminary work we had investigated the contribution of each galaxy to the total far-IR emission of its group and identified 9 of the 14 groups, in which ex-

tended cold dust emission may be present. In the present work, using our larger sample of 32 groups and the physical model of da Cunha et al. (2008) we repeat the same analysis. In Fig. 15 we plot the fraction of the integrated IRAS flux densities at 60 and 100 μm for each group as measured by Allam et al. (1996) divided by the sum of the flux densities of all group members predicted by our SED model fit. The results are presented in Table 7. We identify 13 groups (HCG6, 7, 16, 25, 55, 57, 67, 68, 71, 75, 79, 91 & 95) where diffuse cold dust emission may be present. These results agree with the previous of Bitsakis et al. (2010) with HCG37 be the only exception. Moreover, 10 of these groups are dynamically “old”. This is in agreement with the notion that dynamically “old” groups are more evolved and their members have experienced more encounters enriching the intragroup medium. It is possible that part of the apparent far-IR excess is due to the uncertainties introduced by our SED fits. Only far-infrared imaging with the Herschel Space Telescope will enable us to reliably characterize the composition and structure of the intragroup medium as well as study the evolution of the cold dust in these systems.

5. Conclusions

In this paper we have presented the first multi-wavelength analysis, from the UV to the infrared, of the 135 galaxies which are members of 32 Hickson Compact Groups and studied the influence of the group environment in their evolution. Based on the theoretical modelling of their SEDs we conclude the following:

- The classification of the evolutionary state of HCGs according to the fraction of their early-type members appears to be physical and is in general agreement with previous classifications. The study of their properties suggest that dynamically “old” groups are more compact and have higher velocity dispersions. They also display higher stellar masses than the “young” ones, while both have similar HI mass distributions. However, “old” groups have nearly an order of magnitude larger dynamical masses than “young” groups.
- The late-type galaxies in dynamically “old” groups display lower sSFRs since the multiple past interactions have already converted a fraction of their gas into stars increasing their stellar masses. This is also the main reason why these galaxies show redder NUV/optical colors than field spirals. However, there are few spiral galaxies in these groups which display even redder colors. They all have very small SFRs, similar to early-type systems. We speculate that tidal interactions must have stripped the gas out of their disk suppressing their star formation activity.
- Most early-type galaxies in dynamically “old” groups, seem to migrate from the star-forming to the quiescent galaxy colors, even though a fraction of them (~25%) display bluer colors and higher star formation activity than normal field ellipticals possibly due to gas accretion from other group members as well as merging of dwarf companions.
- Late-type galaxies in dynamically “young” groups have similar star formation properties to field spirals, as well as in early-stage interacting pairs.
- Even though nearly 46% of the HCG members have an optically identified AGN, we find no evidence of enhanced AGN activity at any stage of the group evolution, or the optical/mid-IR colors of the galaxies.
- Our analysis suggests that the reported lower density of galaxies in the IRAC color-color diagram is caused by the morphological natural bimodality of galaxies and it is similar to what is also observed in the UV-optical colors.
- Our SED model suggests that in 13 groups, 10 of which are dynamically “old”, there is diffuse cold dust in the intragroup medium.
- There are 10 galaxies with mid-IR colors, SEDs, and star formation properties which are inconsistent with their optical classification as early-type systems. We suggest that 7 of them are likely nearly edge-on late-type galaxies which were misclassified due to their small size and dust extinction.

Acknowledgements. TB, VC, and TDS would like to acknowledge partial support from the FP7-REGPOT 206469 grant. We would like to thank H.S. Hwang, D. Elbaz and P.-A. Duc (CEA/Saclay, France) for useful discussions which improved the paper, as well as U. Lisenfeld (Univ. of Granada) for providing the CO data for a number of groups prior to publication.

References

- Aguerre, J. A. L., Castro-Rodríguez, N., Napolitano, N., Arnaboldi, M., & Gerhard, O. 2006, *A&A*, 457, 771
- Allam, S., Assendorp, R., Longo, G., Braun, M., & Richter, G. 1996, *A&AS*, 117, 39
- Bahcall, J. N., & Tremaine, S. 1981, *ApJ*, 244, 805
- Bell, E.F., McIntosh, D.H., Katz, N., Weinberg, M.D. 2003, *ApJS*, 149, 289
- Bertin, E., & Arnouts, S. 1996, *A&AS*, 117, 393
- Bertin, E. 2008, SWarp, <http://astromatic.iap.fr/software/swarp>
- Bitsakis, T., Charmandaris, V., Le Floch, E., Díaz-Santos, T., Slater, S. K., Xilouris, E. and Haynes, M. P. 2010, *A&A*, 517, 75B
- Bressan, A., et al. 2006, *ApJ*, 639, L55
- Bicay, M. D., & Giovanelli, R. 1987, *ApJ*, 321, 645
- Bruzual, G. and Charlot, S. 2003, *MNRAS*, 344, 1000B
- Borthakur, S., Yun, M. S., & Verdes-Montenegro, L. 2010, *ApJ*, 710, 385
- Buat, V., et al. 2005, *ApJ*, 619, L51
- Calzetti, D., et al. 2007, *ApJ*, 666, 870
- Chabrier, G. 2003, *PASP*, 115, 763C
- Charlot, S. and Fall, S. M. 2000, *ApJ*, 539, 718C
- da Cunha, E., Charlot, S., Elbaz, D. 2008, *MNRAS*, 388, 1595
- da Cunha, E., Eminian, C., Charlot, S. and Blaizot, J. 2010, *MNRAS*, 403, 1894
- da Cunha, E., Charmandaris, V., Díaz-Santos, T., Armus, L., Marshall, J. A., & Elbaz, D. 2010, *A&A*, 523, A78
- Dale, D. A., et al. 2005, *ApJ*, 633, 857
- Dale, D. A., et al. 2009, *ApJ*, 703, 517
- Fazio, G. G., et al. 2004, *ApJS*, 154, 10
- Haines, C. P., Gargiulo, A., La Barbera, F., Mercurio, A., Merluzzi, P., & Busarello, G. 2007, *MNRAS*, 381, 7
- Haines, C. P., Gargiulo, A. & Merluzzi, P. 2008, *MNRAS*, 385, 1201
- Hernquist, L., Katz, N., & Weinberg, D. H. 1995, *ApJ*, 442, 57
- Hao, L., et al. 2005, *AJ*, 129, 1783
- Hickson, P. 1982, *ApJ*, 255, 382
- Hickson, P., Kindl, E. and Auman, J. R. 1989, *ApJ*, 70, 687
- Hickson, P., Mendes de Oliveira, C., Huchra, J. P., & Palumbo, G. G. 1992, *ApJ*, 399, 353
- Hwang, H. S., Elbaz, D., Lee, J. C., Jeong, W.-S., Park, C., Lee, M. G., & Lee, H. M. 2010, *A&A*, 522, A33
- Iglesias-Páramo, J., et al. 2006, *ApJS*, 164, 38
- Johnson, K. E., Hibbard, J. E., Gallagher, S. C., Charlton, J. C., Hornschemeier, A. E., Jarrett, T. H., & Reines, A. E. 2007, *AJ*, 134, 1522
- Kaneda H., Onaka T., Sakon I., Kitayama T., Okada Y. and Suzuki, T. 2008, *ApJ*, 684, 270
- Kauffmann, G., et al. 2003, *MNRAS*, 346, 1055
- Kennicutt, R. C., Jr., et al. 2003, *PASP*, 115, 928
- Kewley, L. J., Groves, B., Kauffmann, G., & Heckman, T. 2006, *MNRAS*, 372, 961
- Kong, X., Charlot, S., Brinchmann, J., & Fall, S. M. 2004, *MNRAS*, 349, 769
- Leitherer, C., et al. 1999, *ApJS*, 123, 3
- Mamon, G. A. 1986, *ApJ*, 307, 426
- Martinez, M. A., Del Olmo, A., Coziol, R., Perea, J. 2010, *AJ*, 139, 1199
- Martinez-Badenes et al. 2011, *A&A*, (submitted)
- McConnachie, A. W., Ellison, S. L., & Patton, D. R. 2008, *MNRAS*, 387, 1281
- Mendes de Oliveira, C. & Hickson, P. 1994, *ApJ*, 427, 684
- Meurer, G. R., Heckman, T. M., & Calzetti, D. 1999, *ApJ*, 521, 64
- Morrissey, P. and GALEX Science Team 2005, *A&AS*, 20717903M
- Mulchaey, J. S., Davis, D. S., Mushotzky, R. F., & Burstein, D. 2003, *ApJS*, 145, 39

- Y. Okada, N. Murakami, A. Yasuda, N. Takahashi, M. Kawada et al., AKARI FIS Data Users Manual, Version 1.3, <http://www.ir.isas.jaxa.jp/ASTRO-F/Observation/>
- Panuzzo, P., Rampazzo, R., Bressan, A., Vega, O., Annibali, F., Buson, L. M., Clemens, M. S., & Zeilinger, W. W. 2011, A&A, 528, A10
- Park, C. & Hwang, H. S. 2009, ApJ, 699, 1595
- Ponman, T. J., Bourner, P. D. J., Ebeling, H., Bohringer, H. 1996, MNRAS, 283, 690
- Rieke, G. H., et al. 2004, ApJS, 154, 25
- Rosenberg, J. L., Wu, Y., Le Floch, E., Charmandaris, V., Ashby, M. L. N., Houck, J. R., Salzer, J. J., & Willner, S. P. 2008, ApJ, 674, 814
- Salim S., et al. 2007, ApJS, 173, 267
- Shimada, M., Ohyama, Y., Nishiura, S., Murayama, T., & Taniguchi, Y. 2000, AJ, 119, 2664
- Slater, S. K., Charmandaris, V., & Haynes, M. P. 2004, Bulletin of the American Astronomical Society, 36, 728
- Smith, B. J., Struck, C., Hancock, M., Appleton, P. N., Charmandaris, V., & Reach, W. T. 2007a, AJ, 133, 791
- Smith, J. D. T., et al. 2007b, ApJ, 656, 770
- tern, D., et al. 2005, ApJ, 631, 163
- Strateva, I., et al. 2001, AJ, 122, 1861
- Skrutskie, M. F., et al. 2006, AJ, 131, 1163
- Struck, C. 1999, Phys. Rep., 321, 1
- Temi, P., Brighenti, F., Mathews, W. G. 2004, AJ, 633, L25
- Tzanavaris, P., et al. 2010, ApJ, 716, 556
- Verdes-Montenegro, L., Yun, M. S., Williams, B. A., Huchtmeier, W. K., Del Olmo, A., & Perea, J. 2001, A&A, 377, 812
- Véron-Cetty, M.-P., & Véron, P. 2006, A&A, 455, 773
- Walker, L. M., Johnson, K. E., Gallagher, S. C., Hibbard, J. E., Hornschemeier, A. E., Charlton, J. C., & Jarrett, T. H. 2010, Galaxy Wars: Stellar Populations and Star Formation in Interacting Galaxies, 423, 88
- Williams, B. A., McMahon, P. M., & van Gorkom, J. H. 1991, AJ, 101, 1957
- Wyder, T., et al. 2007, ApJ, 173, 293
- Zibetti, S., Charlot, S., & Rix, H.-W. 2009, MNRAS, 400, 1181

Table 1. Summary of available observations.

Filters	No of galaxies	Comments
GALEX FUV, NUV	105, 135	AIS, MIS, and Guest Investigator maps.
B, R	129	from Hickson (1982).
SDSS	79	Model magnitudes of all Sloan filters (<i>ugriz</i>) DR7.
J, H, Ks	128	63 galaxies from Palomar Obs., 4 from Skinakas Obs., and 68 from 2MASS.
Spitzer/IRAC	135	No maps at 3.6 and 5.8 μ m for HCG44b. No maps at 4.5 and 8.0 μ m for HCG68c.
Spitzer/MIPS 24 μ m	124	No maps or undetected: HCG25f, 40f, 57g, 68d, 68e, 75b, 75e, 92d, 92e, 97b and 97e.
IRAS 60, 100 μ m	31	from Allam et al. (1996).
AKARI FIS	26	AKARI FIS source catalogue includes the 65, 90, 140, and 160 μ m photometry.
Optical Spectra	94	from Martinez et al. (2010), Shimada et al. (2000), Hao et al. (2005) and Véron-Cetty & Véron (2006).

Table 2. The UV to IR photometry of our sample.

HCG galaxy	Morphology	Nuclear Classification	Distance Mpc	FUV mJy	NUV mJy	B mJy	R mJy	u mJy	g mJy	r mJy	i mJy	z mJy	J mJy
37a	E7	dLINER	95.8	0.10±0.01	0.38±0.04	11.2±0.56	44.5±2.23	3.26±0.09	18.0±0.54	38.0±1.14	54.5±1.63	71.8±2.15	80.7±2.42
37b	Sbc	LINER	95.8	0.04±0.04	0.11±0.01	2.58±0.13	13.7±0.69	0.58±0.02	3.40±0.10	8.87±0.27	12.9±0.39	19.6±0.59	33.2±1.00
37c	S0a	LLAGN	104.7	0.01±0.00	0.04±0.00	1.03±0.05	4.92±0.25	0.33±0.01	1.64±0.05	3.56±1.07	5.20±0.16	6.92±0.21	8.10±0.24
37d	SBdm	-	87.0	0.10±0.01	0.15±0.01	1.13±0.06	1.32±0.07	0.31±0.01	1.08±0.03	1.67±0.05	2.13±0.06	2.54±0.08	2.74±0.08
37e	E0	TO	91.4	0.01±0.00	0.03±0.00	0.65±0.03	1.20±0.06	0.19±0.00	0.76±0.02	1.19±0.04	1.43±0.04	1.59±0.05	4.00±0.12

H mJy	Ks mJy	3.6 μ m mJy	4.5 μ m mJy	5.8 μ m mJy	8.0 μ m mJy	24 μ m mJy	60 μ m mJy	100 μ m mJy	65 μ m mJy	90 μ m mJy	140 μ m mJy	160 μ m mJy	References
79.6±2.39	88.1±2.64	61.7±1.85	37.2±1.12	19.3±0.58	13.4±0.40	4.80±0.24	490±49	2000±200	-	-	-	-	a2,b1,c1
43.3±1.30	43.6±1.30	22.9±0.68	14.4±0.43	14.5±0.44	29.1±0.87	36.7±1.84	561±56	-	675±34	725±36	2156±107	2445±122	a2,b1,c1
8.90±0.27	7.40±0.22	3.50±0.11	2.30±0.07	1.80±0.05	2.10±0.06	3.50±0.18	190±19	-	-	-	-	-	a2,b1,c1
3.45±0.10	3.19±0.10	1.84±0.06	1.14±0.03	2.01±0.06	5.19±0.16	4.90±0.25	-	-	-	-	-	-	a2,b1,c1
5.18±0.15	4.77±0.14	2.41±0.07	1.48±0.04	1.02±0.03	1.07±0.03	1.80±0.09	-	-	-	-	-	-	a1,b1,c1

Notes. ^(a1,2,3,4) The nuclear classification obtained from Martinez et al. (2010), Shimada et al. (2000), Hao et al. (2005) and Véron-Cetty & Véron (2006) respectively. ^(b1,2,3) The near-IR photometry from Palomar, 2MASS and Skinakas respectively. ^(c1,2,3,4,5,6) The mid-IR photometry from Bitsakis et al. (2010), Johnson et al. (2007), and the Spitzer archive (PIDs: 50764, 159, 40385, 198) respectively. The complete table is available by the authors upon request.

Table 3. Observational Parameters of Spitzer Archival Data

HCG ID	R.A. (J2000)	Dec. (J2000)	z	IRAC ^a sec	MIPS ₂₄ ^a sec	Observer PID
HCG4	00h34m15.9s	-21d26m48s	0.0269	10.0	18.3	40385
HCG6	00h39m10.1s	-08d23m43s	0.0379	150.0	375.4	50764
HCG15	02h07m39.0s	+02d08m18s	0.0228	300.0	375.4	50764
HCG25	03h20m43.7s	-01d03m07s	0.0212	300.0	375.4	50764
HCG44	10h18m00.5s	+21d48m44s	0.0046	360.0	917.5	159
HCG67	13h49m03.5s	-07d12m20s	0.0245	300.0	375.4	50764
HCG68	13h53m40.9s	+40d19m07s	0.0080	75.0	375.4	50764
HCG75	15h21m33.8s	+21d11m00s	0.0416	150.0	375.4	50764
HCG82	16h28m22.1s	+32d49m25s	0.0362	150.0	375.4	50764
HCG91	22h09m10.4s	-27d47m45s	0.0238	300.0	375.4	50764
HCG92	22h35m57.5s	+33d57m36s	0.0215	432.0	627.5	198
HCG97	23h47m22.9s	-02d19m34s	0.0218	300.0	375.4	50764
HCG100	00h01m20.8s	+13d07m57s	0.0178	300.0	375.4	50764

Notes. ^(a) On source integration time for each of the four IRAC filters and MIPS 24 μ m filter.

Table 4. The morphological type and derived physical parameters based on the SED modeling of the HCG galaxies

HCG galaxy	Morphological Type	χ^2	$\tau_{V,obs}$	$\tau_{V,ISM}$	$\tau_{V,BC+ISM}$	M_{star} $\times 10^9 M_{\odot}$	SFR $M_{\odot} \text{yr}^{-1}$	sSFR $\times 10^{-11} \text{yr}^{-1}$	L_{IR} $\times 10^9 L_{\odot}$
2a*	SBd	2.38	0.11	0.05	0.67	3.86	2.18	57.81	14.45
2b	cl	2.96	0.52	0.42	1.16	3.56	1.75	48.64	32.35
2c	SBc	1.66	0.17	0.10	0.64	4.24	0.43	10.28	3.17
4a*	Sc	5.47	0.36	0.16	1.60	69.18	7.29	10.52	169.8
4b	Sc	5.22	0.13	0.11	0.63	7.62	0.41	5.37	4.09
4d	E4	5.96	0.53	0.51	0.94	12.88	0.96	7.41	1.46
6a*	S0a	2.65	0.13	0.14	1.98	87.1	0.01	0.01	15.84
6b*	Sab	5.69	0.24	0.23	1.45	77.62	0.05	0.07	21.87
6c	E5	5.49	0.10	0.10	0.70	58.88	0.01	0.01	4.38
6d	Sbc	1.38	0.19	0.09	0.32	3.78	0.07	2.19	6.05
7a*	Sb	2.07	0.61	0.57	2.27	74.13	1.65	2.19	2.40
7b	SB0	3.58	0.17	0.17	1.68	38.90	0.14	0.36	0.77
7c	SBc	4.37	0.34	0.33	0.38	23.44	1.61	6.92	33.88
7d	SBc	8.61	0.03	0.02	0.65	8.85	0.32	3.16	4.38
15a	Sa	5.59	0.09	0.10	0.64	81.28	0.10	0.11	14.45
15b	E0	4.60	0.24	0.24	0.82	40.74	0.05	0.11	2.40
15c*	E0	8.73	0.07	0.08	0.42	107.15	0.02	0.02	3.86
15d	E2	2.06	0.48	0.18	1.35	24.55	0.01	0.32	8.64
15e	Sa	7.30	0.44	0.03	0.67	25.70	0.06	0.22	3.99
15f	Sbc	7.65	0.81	0.14	0.30	2.07	0.28	14.03	2.67
16a	Sba	5.95	0.92	0.85	2.65	50.12	4.14	7.76	0.63
16b*	Sab	3.41	0.12	0.11	2.19	63.10	0.04	0.07	1.78
16c	Im	2.11	1.09	0.99	2.25	11.75	8.18	69.5	72.4
16d	Im	6.86	1.26	1.14	2.72	30.20	1.45	4.79	2.61
22a*	E2	2.19	0.10	0.09	0.31	70.79	0.01	0.07	100.0
22b	Sa	2.55	0.24	0.17	0.38	5.52	0.01	0.06	89.12
22c	SBc	4.02	0.22	0.08	0.26	3.37	0.19	7.76	1.48
25a	SBc	5.86	0.29	0.54	1.13	13.18	9.61	71.94	3.48
25b*	SBa	5.62	0.03	0.03	0.31	69.18	0.16	0.23	0.85
25d	S0	3.58	0.14	0.14	3.40	11.48	0.05	0.58	3.06
25f*	S0	4.24	0.04	0.04	0.15	8.17	0.05	0.60	0.17
37a*	E7	5.26	0.24	0.24	0.45	128.82	0.18	0.14	1.38
37b	Sbc	4.15	0.74	0.73	3.63	74.13	0.58	0.78	26.91
37c	SBd	3.86	0.73	0.71	3.56	17.38	0.08	0.46	1.41
37d	SBdm	4.70	0.24	0.25	1.77	0.89	0.15	17.66	75.85
37e	E0	5.26	0.21	0.20	0.70	1.65	0.03	1.95	1.20
38a	Sbc	3.40	1.03	0.95	3.53	46.77	2.18	4.68	23.44
38b*	SBd	7.82	1.06	1.17	3.07	50.12	4.60	8.51	0.34
38c	Im	2.49	1.07	1.03	2.87	23.44	1.40	5.62	0.75
40a*	E3	0.85	0.57	0.57	2.10	165.96	0.22	0.13	38.90
40b	S0	2.30	0.89	0.87	1.65	83.18	0.36	0.43	12.88
40c	Sbc	4.24	1.46	1.13	3.64	69.18	2.39	3.47	3.21
40d	SBa	3.02	1.07	1.02	3.79	52.48	0.59	1.12	45.70
40e	Scd	3.65	1.50	1.40	2.33	14.13	0.66	4.27	5.03
40f*	E1	5.13	0.02	0.02	0.58	6.64	0.01	0.01	1.00
42a*	E3	3.38	0.15	0.15	1.09	245.47	0.05	0.02	2.58
42b	SB0	7.92	0.16	0.15	1.09	25.12	0.01	0.01	16.21
42c	E2	2.66	0.46	0.15	1.87	20.89	0.02	0.09	20.89
42d	E2	2.54	0.35	0.03	0.67	3.52	0.01	0.13	77.62
44a*	Sa	11.89	0.34	0.34	2.29	36.31	0.07	0.20	7.62
44b	E2	7.09	0.38	0.38	0.66	19.95	0.03	0.17	17.78
44c	SBc	3.93	0.29	0.29	0.54	5.46	0.11	2.09	22.90
44d	Sd	8.52	0.31	0.31	0.57	0.64	0.63	98.17	7.53
47a*	Sbc	10.46	0.54	0.53	0.76	95.5	3.07	3.16	1.74
47b	E3	9.66	0.34	0.33	0.57	75.86	0.30	0.39	0.70
47c	Scd	3.33	1.04	1.01	3.27	15.14	0.93	6.03	43.65
47d	Sdm	3.63	0.14	0.13	0.22	16.98	0.48	2.75	104.71
54a*	Sdm	7.78	1.84	1.84	3.34	0.39	3.07	16.53	34.67
54b	Im	5.67	1.41	1.31	1.74	0.07	0.20	49.26	0.78
54c	Im	2.35	1.13	0.61	1.19	0.02	0.08	23.44	40.73
54d	Im	4.36	0.98	0.30	2.48	0.01	0.03	32.51	33.88
55a	E0	5.80	0.36	0.35	0.81	93.33	0.40	0.42	64.56
55b	S0	4.03	0.26	0.17	1.87	70.79	0.02	0.03	36.30
55c*	E3	1.68	0.94	1.01	2.96	112.2	1.17	1.05	14.45
55d	E2	2.89	0.18	0.18	0.98	30.20	0.08	0.26	0.07
56a	Sc	4.68	0.52	0.51	0.54	17.78	0.70	3.89	12.58
56b*	SB0	17.21	1.34	1.29	2.75	34.67	1.69	4.79	2.17
56c	S0	8.28	0.22	0.03	0.40	26.30	0.05	0.20	4.69

Notes. (*) Galaxies marked with a star are the most massive of each group and were used in the calculations of the dynamical masses in Table 5.
 (*) Galaxies with no $24\mu\text{m}$ data. The SFRs, sSFRs and L_{IR} of these systems are not well constrained. (*) In these galaxies the presence of an AGN into their nucleus dominates their mid-IR emission.

HCG galaxy	Morphological Type	χ^2	$\tau_{V,obs}$	$\tau_{V,ISM}$	$\tau_{V,BC+ISM}$	M_{star} $\times 10^9 M_{\odot}$	SFR $M_{\odot} \text{yr}^{-1}$	sSFR $\times 10^{-11} \text{yr}^{-1}$	L_{IR} $\times 10^9 L_{\odot}$
56d	S0	5.05	1.01	0.98	1.69	10.23	0.42	4.07	0.08
56e	S0	4.91	0.32	0.31	0.71	4.29	0.23	5.37	4.04
57a*	Sbc	7.75	0.28	0.29	1.20	177.83	0.76	0.43	4.33
57b	SBb	4.15	0.28	0.28	0.52	83.18	0.49	0.60	1.43
57c	E3	4.00	0.06	0.05	0.66	87.10	0.01	0.01	1.80
57d	SBc	2.31	0.22	0.18	1.64	13.80	1.77	12.22	46.77
57e	S0a	4.74	0.89	0.87	1.86	91.20	0.19	0.20	11.48
57f	E4	3.28	0.40	0.33	1.96	52.48	0.03	0.05	27.54
57g*	SB0	2.66	0.09	0.09	0.26	44.67	0.05	0.10	3.40
57h	SBb	6.18	0.30	0.21	2.13	12.59	0.09	0.71	3.36
59a*	Sa	19.03	0.28	0.25	2.06	14.79	0.06	0.43	4.75
59b	E0	7.77	0.03	0.03	0.59	7.19	0.01	0.06	0.88
59c	Sc	1.92	0.23	0.11	0.63	1.34	0.10	8.13	0.77
59d	Im	6.48	1.47	0.16	1.81	0.78	0.57	72.78	0.65
61a*	S0a	4.37	0.63	0.62	3.08	89.13	0.16	0.17	11.22
61c	Sbc	2.30	1.30	1.23	3.74	45.71	1.79	3.80	2.99
61d	S0	1.58	0.02	0.02	0.29	23.44	0.04	0.17	0.33
62a*	E3	1.74	0.16	0.16	1.33	91.20	0.03	0.03	0.55
62b	S0	4.60	0.10	0.10	0.70	35.48	0.01	0.01	0.68
62c	S0	5.48	0.17	0.17	0.69	22.39	0.02	0.07	22.90
62d	E2	4.89	0.39	0.39	0.68	5.92	0.03	0.48	7.03
67a*	E1	6.70	0.12	0.12	0.46	245.47	0.02	0.07	2.09
67b	Sc	8.25	1.13	1.07	2.23	23.99	1.13	4.47	1.22
67c	Scd	4.25	0.58	0.14	0.51	14.45	0.55	3.98	0.50
67d	S0	0.19	0.10	0.06	0.79	14.79	0.05	0.32	23.98
68a	S0	14.93	0.02	0.02	0.09	67.61	0.31	0.46	4.48
68b	E2	6.05	0.13	0.11	2.28	60.26	0.06	0.09	42.65
68c*	SBbc	4.95	0.36	0.36	0.96	70.79	0.05	0.07	3.73
68d*	E3	6.22	0.14	0.05	1.15	9.06	0.01	0.10	54.95
68e*	S0	3.83	0.07	0.03	0.59	5.71	0.01	0.06	10.23
71a*	Sbc	5.22	0.25	0.16	0.28	69.18	1.65	2.34	77.62
71b	SB0	7.41	1.17	1.13	3.23	40.74	1.34	3.31	1.30
71c	Sbc	4.74	0.18	0.17	0.48	7.28	0.53	7.24	15.48
75a*	E4	6.84	0.14	0.14	1.39	204.17	0.26	0.13	4.18
75b*	Sb	8.62	0.03	0.03	0.04	33.11	0.01	0.01	23.44
75c	S0	6.18	0.21	0.18	0.46	56.23	0.02	0.06	13.80
75d	Sd	4.39	0.45	0.29	1.09	23.44	0.65	2.75	1.80
75e*	Sa	1.72	0.01	0.04	0.24	45.71	0.06	0.14	19.05
79a*	Sa	6.76	0.66	0.65	1.85	36.31	0.10	0.26	30.90
79b	S0	5.90	0.99	0.77	2.14	34.67	0.14	0.35	9.59
79c	S0	6.83	0.44	0.43	1.16	4.49	0.01	0.28	1.61
79d	Sdm	3.36	1.34	1.15	2.13	0.74	3.74	48.08	1.98
82a*	E3	5.11	0.39	0.38	0.70	208.93	0.07	0.03	8.35
82b	SBa	4.75	0.78	0.76	1.72	123.03	0.15	0.12	0.12
82c	Im	4.86	1.04	0.99	3.94	33.88	3.25	9.55	0.86
82d	S0a	8.11	0.05	0.05	1.15	28.18	0.03	0.10	54.95
91a*	SBc	7.59	0.41	0.39	0.56	91.2	10.16	11.02	26.91
91b	Sc	2.41	1.01	0.88	1.80	27.54	5.22	18.49	53.70
91c	Sc	4.73	0.16	0.08	0.65	14.79	3.22	21.48	0.41
91d	SB0	0.95	0.40	0.04	0.39	22.39	0.26	1.10	4.33
92a	Sc	3.74	0.23	0.23	0.65	11.75	0.79	6.76	1.40
92b	SBbc	5.97	0.71	0.62	0.81	38.02	2.23	5.89	1.84
92c*	SBbc	5.05	2.27	2.20	3.60	39.81	26.42	64.86	1.48
92d*	E2	5.94	0.35	0.08	0.32	34.67	0.12	0.35	7.19
92e*	E4	3.72	0.37	0.01	0.07	64.57	0.01	0.01	43.66
95a*	Sbc	8.10	0.87	0.83	1.73	131.83	2.25	1.70	5.78
95c	Sbc	5.08	1.66	1.47	3.06	16.6	14.52	87.5	0.89
95d	SB0	2.25	0.64	0.61	1.41	45.71	0.96	2.14	1.22
97a*	E5	2.89	0.03	0.03	0.04	81.28	0.01	0.02	2.96
97b*	Sc	1.95	0.78	0.44	0.99	16.98	0.55	2.75	11.22
97c	Sa	6.61	0.14	0.14	2.05	23.44	0.02	0.07	0.23
97d	E1	1.46	0.03	0.02	0.13	47.86	0.04	0.09	0.20
97e*	S0a	5.10	0.09	0.02	0.21	9.82	0.02	0.17	15.84
100a*	S0a	2.54	0.25	0.20	1.53	61.66	1.05	1.70	60.25
100b	S	3.56	0.52	0.50	2.08	5.65	0.34	5.89	4.86
100c	S	3.78	1.54	0.45	1.80	2.44	1.67	67.92	5.98
100d	Scd	1.96	0.29	0.08	0.69	0.57	0.11	20.28	10.96

Notes. (*) Galaxies marked with a star are the most massive of each group and were used in the calculations of the dynamical masses in Table 5. (•) Galaxies where no 24 μ m observations were available and so their SFRs, sSFRs and L_{IR} are not well constrained. (•) In these galaxies the presence of an AGN into their nucleus dominates their IR emission.

Table 5. Derived physical parameters based on the SED modelling of the interacting pair galaxy sample

Galaxy	z	$\tau_{V,obs}$	$\tau_{V,ISM}$	$\tau_{V,BC+ISM}$	M_{star} $\times 10^9 M_{\odot}$	SFR $M_{\odot} yr^{-1}$	sSFR $\times 10^{-11} yr^{-1}$	L_{IR} $\times 10^9 L_{\odot}$
Arp24a	0.0069	0.21	0.06	0.59	0.05	0.05	74.47	0.17
Arp24b	0.0069	0.46	0.49	1.29	0.68	5.22	948.4	48.98
Arp34a	0.0157	0.32	0.16	0.81	4.90	1.50	30.20	12.3
Arp34b	0.0157	0.62	0.21	1.26	30.20	0.34	1.23	6.64
Arp65a	0.0179	0.95	0.90	2.81	34.67	1.12	3.16	39.81
Arp65b	0.0179	0.23	0.20	1.13	19.50	0.35	1.82	5.78
Arp72a	0.0109	0.89	0.17	0.96	2.28	3.98	165.9	30.9
Arp72b	0.0109	0.44	0.06	0.34	0.21	0.33	164.8	2.44
Arp82a	0.0136	0.23	0.26	1.85	18.62	2.39	12.59	29.51
Arp82b	0.0136	0.66	0.18	0.93	3.09	0.67	23.01	6.56
Arp84a	0.0115	1.12	1.16	2.47	9.33	3.56	36.31	51.29
Arp84b	0.0115	0.40	0.48	1.73	61.66	3.82	6.31	57.54
Arp85a	0.0015	0.31	0.48	2.07	9.12	0.05	0.60	3.61
Arp85b	0.0015	0.45	0.47	1.68	8.71	2.39	25.82	27.54
Arp86a	0.0172	0.29	0.34	1.79	114.82	4.09	3.63	63.1
Arp86b	0.0172	1.45	0.88	3.03	2.95	4.14	120.23	41.69
Arp87a	0.0235	0.86	0.90	2.00	9.77	3.98	38.90	54.95
Arp87b	0.0235	0.26	0.22	1.14	16.60	2.28	13.80	22.91
Arp89a	0.0068	0.21	0.17	1.44	0.66	0.16	23.28	1.31
Arp89b	0.0068	1.26	0.63	2.02	41.69	0.16	0.40	18.62
Arp120a	0.0026	0.25	0.25	1.75	11.20	0.09	0.08	1.75
Arp120b	0.0026	0.44	0.38	1.52	17.80	0.16	0.91	5.4
Arp181a	0.0315	0.72	0.29	1.20	97.72	2.24	2.40	37.15
Arp181b	0.0315	0.96	0.86	2.00	52.48	3.33	6.31	81.28
Arp202a	0.0102	1.00	0.30	1.04	0.66	1.67	234.4	11.75
Arp202b	0.0102	0.87	0.17	0.75	0.89	1.40	363.1	29.51
Arp242a	0.0220	1.03	0.93	3.00	43.65	3.03	7.24	50.12
Arp242b	0.0220	0.14	0.23	1.25	39.81	1.12	2.88	12.3
Arp244a	0.0054	0.29	0.30	1.56	26.3	4.45	16.29	54.95
Arp244b	0.0054	0.99	0.81	2.60	89.13	2.44	3.80	83.18
Arp271a	0.0087	0.08	0.19	0.96	12.88	7.19	54.95	58.88
Arp271b	0.0087	0.43	0.29	1.54	6.03	3.65	61.66	32.36
Arp280a	0.0024	0.93	0.72	2.00	0.02	0.15	916.2	1.57
Arp280b	0.0024	0.08	0.05	2.62	2.09	0.17	8.13	1.52
Arp282a	0.0154	0.49	0.48	2.20	85.11	0.42	0.54	19.05
Arp282b	0.0154	0.45	0.26	1.31	7.24	0.43	6.03	5.65
Arp283a	0.0055	0.07	0.11	0.82	1.23	0.17	15.38	1.52
Arp283b	0.0055	1.19	1.11	2.91	12.02	1.91	15.85	35.48
Arp284a	0.0092	0.80	0.10	0.55	0.81	0.07	8.13	0.56
Arp284b	0.0092	1.14	0.49	2.12	2.04	6.46	275.4	57.54
Arp285a	0.0087	0.76	0.81	2.32	18.62	1.14	5.75	26.3
Arp285b	0.0087	0.31	0.41	1.94	8.71	0.85	9.55	11.48
Arp290a	0.0121	0.29	0.21	1.41	29.51	0.44	1.51	5.92
Arp290b	0.0121	1.01	0.65	2.58	28.18	0.02	0.09	7.19
Arp295a	0.0220	1.06	0.89	3.30	7.76	11.48	144.5	114.82
Arp295b	0.0220	0.76	0.71	2.22	26.92	0.54	2.29	30.2
Arp297a	0.0322	0.17	0.12	0.68	31.62	1.23	3.72	12.02
Arp297b	0.0322	0.74	0.58	1.67	5.62	0.63	11.27	10.47
Arp298a	0.0163	0.85	1.02	2.77	14.79	2.09	13.80	33.88
NGC4567a	0.0163	1.92	1.14	3.35	114.82	28.84	25.12	1047.13
NGC4567b	0.0074	1.06	0.88	3.05	58.88	6.03	11.22	138.04

Notes. We calculate the two components of τ_V using: $\tau_{V,ISM} = \mu \tau_V$ and $\tau_{V,BC} = (1 - \mu) \tau_V$.

Table 6. Distance to, virial radius and morphology of the nearest neighbor as well as “strength” of interaction for the HCG galaxies.

HCG galaxy	R ^a kpc	r _{vir} ^b kpc	<R/r _{vir,nei} >/n ^c	type of ^d nearest neighbor
2a	24	404	0.092	late
2b	24	357	0.108	late
2c	76	255	0.673	late
4a	62	662	0.085	late
4b	28	467	0.041	early
4d	28	399	0.070	late
6a	37	745	0.047	early
6b	13	571	0.023	late
6c	13	528	0.025	late
6d	35	293	0.028	late
7a	36	523	0.043	late
7b	21	458	0.038	late
7c	76	452	0.058	late
7d	21	551	0.032	early
15a	101	736	0.055	early
15b	64	529	0.028	late
15c	49	868	0.030	early
15d	14	507	0.034	late
15e	64	591	0.043	early
15f	14	406	0.020	early
16a	16	563	0.032	late
16b	16	488	0.038	late
16c	37	462	0.034	late
16d	37	611	0.047	late
22a	37	555	0.070	late
22b	17	267	0.034	late
22c	17	285	0.034	late
25a	57	552	0.059	early
25b	9	667	0.032	early
25d	46	334	0.041	late
25f	9	310	0.029	late
37a	17	932	0.037	early
37b	20	455	0.039	late
37c	29	449	0.032	early
37d	20	245	0.037	late
37e	30	150	0.037	late
38a	87	437	0.104	late
38b	9	511	0.056	late
38c	9	399	0.060	late
40a	14	795	0.008	late
40b	12	685	0.008	late
40c	12	774	0.007	early
40d	20	760	0.012	early
40e	13	491	0.006	early
42a	21	998	0.034	early
42b	81	583	0.067	early
42c	21	510	0.041	early
42d	31	288	0.031	early
44a	26	335	0.044	late
44b	26	393	0.069	late
44c	54	348	0.078	late
44d	26	213	0.044	late
47a	34	778	0.052	early
47b	34	554	0.034	late
47c	15	389	0.028	late
47d	15	405	0.025	late
54a	1	147	0.007	late
54b	1	152	0.011	late
54c	1	110	0.005	late
54d	1	87	0.006	late
55a	23	929	0.015	early
55b	17	710	0.019	early
55c	17	790	0.015	early
55d	23	588	0.019	early
56a	59	476	0.046	early

Notes. ^(a) Projected distance to the nearest neighbor. ^(b) Virial radius. ^(c) “Strength” of interaction as described in Section 4.6. ^(d) Morphology of the nearest neighbor.

HCG galaxy	R ^a kpc	r _{vir} ^b kpc	<R/r _{vir,nei} >/n ^c	morphology of ^d nearest neighbor
56b	31	622	0.027	early
56c	12	580	0.021	early
56d	12	402	0.022	early
56e	27	436	0.030	early
57a	13	669	0.031	late
57b	26	748	0.020	early
57c	26	583	0.031	late
57d	13	252	0.020	late
57e	32	516	0.028	late
57f	86	641	0.060	early
57g	26	463	0.022	late
57h	32	421	0.025	early
59a	13	368	0.036	late
59b	33	298	0.066	late
59c	26	232	0.046	late
59d	13	182	0.035	late
61a	43	705	0.043	early
61c	24	805	0.033	early
61d	24	400	0.023	late
62a	6	745	0.023	early
62b	6	500	0.025	early
62c	19	518	0.028	early
62d	56	354	0.035	early
67a	17	1032	0.028	early
67b	99	635	0.054	late
67c	25	624	0.031	early
67d	17	486	0.028	early
68a	10	710	0.032	early
68b	10	629	0.030	early
68c	33	532	0.038	early
68d	49	370	0.027	early
68e	47	337	0.037	early
71a	68	799	0.082	early
71b	68	502	0.066	late
71c	76	431	0.064	early
75a	3	920	0.033	early
75b	3	534	0.033	late
75c	23	498	0.032	late
75d	23	533	0.025	early
75e	41	453	0.023	late
79a	4	168	0.006	late
79b	8	523	0.013	early
79c	4	366	0.009	early
79d	5	229	0.009	late
82a	47	789	0.054	late
82b	66	819	0.097	early
82c	44	171	0.028	early
82d	44	440	0.053	late
91a	15	1047	0.039	early
91b	82	662	0.057	late
91c	15	553	0.031	early
91d	15	527	0.032	late
92a	5	629	0.019	late
92b	1	649	0.013	early
92c	4	925	0.020	late
92d	1	663	0.013	late
92e	5	801	0.024	early
95a	20	914	0.032	late
95c	20	726	0.030	late
95d	48	510	0.031	late
97a	37	757	0.031	early
97b	112	568	0.054	early
97c	75	528	0.043	early
97d	37	682	0.034	early
97e	41	442	0.038	early
100a	28	621	0.036	late
100b	34	506	0.056	early
100c	43	394	0.047	late
100d	28	254	0.031	early

Notes. ^(a) Projected distance to the nearest neighbor. ^(b) Virial radius. ^(c) “Strength” of interaction as described in the text. ^(d) Morphology of the nearest neighbor.

Table 7. Observed and predicted $60\mu\text{m}$ and $100\mu\text{m}$ IRAS fluxes for each group, as well as total HI, H_2 , stellar, and dynamical masses

HCG ID	Evolve Class ^a	HI Class ^c	Group members	$f_{60,pred}$ Jy	$f_{60,obs}$ Jy	$f_{100,pred}$ Jy	$f_{100,obs}$ Jy	$\log(M_{\text{HI}})^d$ M_\odot	$\log(M_{\text{star}})$ M_\odot	$\log(M_{\text{H}_2})^e$ M_\odot	$\log(M_{\text{dyn}})$ M_\odot	$(M_{\text{bar}}/M_{\text{dyn}})^f$
2	young	-	3	6.33	6.16	4.03	2.89	10.33	10.07	-	11.67	0.07
4	young ^b	-	3	8.21	8.56	4.35	4.09	10.31	10.95	-	11.96	0.12
6	old	-	4	0.34	0.46	0.11	0.13	9.69	11.36	-	12.66	0.05
7	young	1	4	8.32	9.20	3.42	4.43	9.68	11.16	<9.88	11.64	0.35
15	old	3	6	1.29	0.38	0.94	0.13	9.41	11.14	<9.73	13.24	0.01
16	young	2	4	35.72	62.37	24.04	25.21	>10.42	11.19	10.41	12.57	>0.06
22	old	-	3	2.72	1.48	1.0	1.05	9.13	10.90	-	11.33	0.38
25	old	2	4	1.4	5.21	0.68	1.74	9.90	11.00	<9.61	11.13	0.83
37	old	3	5	2.73	2.60	1.22	0.89	9.19	11.34	9.88	13.01	0.02
38	young	-	3	7.09	3.60	3.16	1.63	9.69	11.08	-	11.31	0.61
40	old	3	6	4.82	3.85	3.42	1.35	9.14	11.59	10.07	12.29	0.21
42	old	-	4	5.14	-	1.66	0.0	9.40	11.47	-	13.17	0.02
44	young	3	4	15.68	14.32	8.28	5.69	9.23	10.79	<9.17	12.70	0.01
47	young	-	4	1.66	1.51	0.82	1.27	9.93	11.30	-	11.63	0.48
54	young	-	4	2.02	1.71	0.35	0.38	8.75	8.69	-	11.25	0.01
55	old	-	4	1.1	1.63	0.26	0.2	-	11.47	-	12.53	0.09
56	old	-	5	2.59	2.27	1.13	0.89	9.36	10.97	-	12.81	0.02
57	old	-	8	3.14	3.54	1.16	1.44	9.71	11.75	-	12.58	0.15
59	young	-	4	13.3	4.83	6.91	3.98	9.49	10.38	-	12.25	0.02
61	old	-	3	16.3	12.45	7.18	6.39	9.96	11.20	-	12.33	0.08
62	old	-	4	1.45	0.72	0.29	0.13	<9.06	11.19	-	12.85	<0.02
67	old	1	4	2.98	2.91	1.15	2.26	10.03	11.48	<10.04	12.16	0.21
68	old	3	5	4.97	10.45	2.08	2.74	9.62	11.33	<9.23	12.82	0.03
71	young ^b	-	3	2.75	3.69	1.29	1.84	-	11.07	-	11.55	0.33
75	old	-	5	1.4	2.15	0.16	0.57	-	11.56	-	12.74	0.07
79	old	1	4	2.89	3.80	2.28	1.41	9.30	10.88	<9.31	11.72	0.15
82	old	-	4	3.92	3.31	0.96	3.47	<9.69	11.60	-	13.04	<0.04
91	young	2	4	8.78	6.11	5.0	2.31	10.32	11.19	-	12.67	0.04
92	old	3	5	7.15	6.57	1.34	1.39	10.02	11.28	-	12.82	0.03
95	old	-	3	9.44	2.39	2.48	6.94	>10.10	11.29	-	12.70	>0.04
97	old	3	5	5.28	-	2.12	0.0	9.10	11.25	<9.80	13.02	0.02
100	young	2	4	5.78	6.46	2.71	2.36	9.74	10.85	<9.37	11.16	0.54

Notes. ^(a) The dynamically “young” and “old” classification as discussed in Section 4.1 and in Bitsakis et al. (2010).

^(b) The original classifications of HCG4 and HCG71 were dynamically “old”, but changed as explained in Section 4.3.

^(c) The classification to Phase 1, 2, and 3, follows the definition of Verdes-Montenegro et al. (2001).

^(d) The upper and lower limits, in HI masses, have been taken into account by means of survival analysis.

^(e) The H_2 masses were obtained from Martínez-Badenes et al. (2011).

^(f) Ratio of the total baryonic mass $M_{\text{bar}}=M_{\text{star}}+M_{\text{HI}}+M_{\text{H}_2}$ over the dynamical mass M_{dyn} .

Appendix A: Peculiar early type systems

As we mentioned in Section 4.4, there are 10 peculiar early-type galaxies which display “red” mid-IR colors. It was suggested that they could either be misclassified late-type systems or that they are indeed early-type which have increased their gas and dust due to interactions and merging with companion galaxies. As we discussed in Section 4.2, some of them display high A_V , SFR, and sSFR. In this section we present all available evidence and we discuss in detail their properties.

In order to better probe their morphology, we first examine how the old stellar populations, traced by their near-IR emission, as well as the warm dust seen in the mid-IR are distributed in each galaxy. In Fig. A.1 we present the “true color” images constructed using the Spitzer/IRAC 3.6, 4.5 and $8.0\mu\text{m}$ maps as the blue, green, and red channel respectively. We also include contour maps of the Ks emission for these galaxies. Bona fide early-type systems should be relaxed dynamically with an $R^{1/4}$ radial profile and elliptical structure in their stellar light emission. Furthermore, they should not display star formation or color gradients hence no variation would be expected in their mid-IR “true color” images. Indeed, when one observes the “true color” image of NGC1404 (a typical field elliptical galaxy) no obvious mid-IR color gradient is seen while the contours of the Ks-band emission, dominated by the old stellar population are concentric ellipses. HCG40f and HCG68a, also display similar mid-IR colors and profiles with the second having Ks contours consistent with a lenticular galaxy. However the rest of the early-type HGC galaxies show either color gradients, or patchy emission in their “true color” mid-IR images, which indicate possible on-going star formation warming up the dust and exciting the PAH molecules in these wavelengths. In particular the galaxies HCG4d, HCG55c, HCG56d, HCG71b and HCG79b display reddish colors which imply stronger $8\mu\text{m}$ emission. In HCG100a the $8.0\mu\text{m}$ emission seems to emerge from two spiral-like structures. Yet when we closely examine the distribution of their old stellar population it appears relaxed. With the exception of HCG56b and HCG71b which display a barred-like structure, no other system shows obvious signs of spiral or irregular structure, even though it would have been challenging to identify such features in edge-on late type systems.

An additional tool which can help us classify these galaxies is their global SEDs and current star formation activity. In Fig. A.2 we present their SEDs and contrast it with the NGC1404, a typical E1 galaxy the SED of which was also fitted with the da Cunha et al. (2008) model. We note that HCG40f and HCG68a display SEDs which are consistent with that of an elliptical galaxy. It is very possible that HCG68a has “red” mid-IR colors because of the existence of an AGN into its nucleus (see Table A. 1). HCG40f was not classified by Hickson (1982) but by us (Bitsakis et al. 2010), since its morphology and SED were consistent an early-type galaxy. However, this galaxy is very close to its neighbor (HCG40d) and it is possible that this could slightly affect its mid-IR colors. The SED of HCG56b is strongly affected by the emission of its Sy2 nucleus which dominates its mid-IR colors. Since our model cannot account for emission due to an AGN we can not draw a firm conclusion on its nature. Among the galaxies for which nuclear optical spectra were available four systems: HCG56d, HCG68a, HCG79b and HCG100a display signatures of an AGN or a transition object, while HCG56e and HCG71b are classified as pure star forming. The remaining of the galaxies display SEDs which are similar with those of late-type galaxies. They have strong mid-IR fluxes consistent with the presence of PAH emission.

With the exception of HCG40f, all nine galaxies have high sSFRs similar to those of late-type systems (see Table A. 1). More specifically HCG4d, HCG55c, HCG56b, HCG56d, HCG56e, HCG71b and HCG100a have sSFRs which are two orders of magnitude larger than what is seen in normal ellipticals, while HCG68a and HCG79b have sSFRs that are just a factor of ten higher. Finally, as we mentioned in Section 4.5, if these galaxies were passively evolving they would display “red” NUV-r colors ($>5\text{mag}$). However, the observed NUV-r colors of HCG4d and HCG56b are blue. After correcting for the dust extinction seven of the remaining of the galaxies also move to the “blue cloud”. It is thus possible that these galaxies are dust obscured late-types with some on-going star formation activity. As a result they display higher sSFRs, “bluer” colors in the UV-optical and “redder” in the mid-IR wavelengths. Even after extinction correction HCG40f remains in the “red sequence” while HCG68a is found in the “green valley”. These galaxies are early-type galaxies which display red mid-IR colors probably because they increased their dust content due to interactions with their neighbors (HCG40d and HCG68b, respectively).

Taking in account all the evidence mentioned above we suggest that HCG4d, HCG55c, HCG56d, HCG56e, HCG71b, HCG79b and HCG100a could be misclassified edge-on late-type systems.

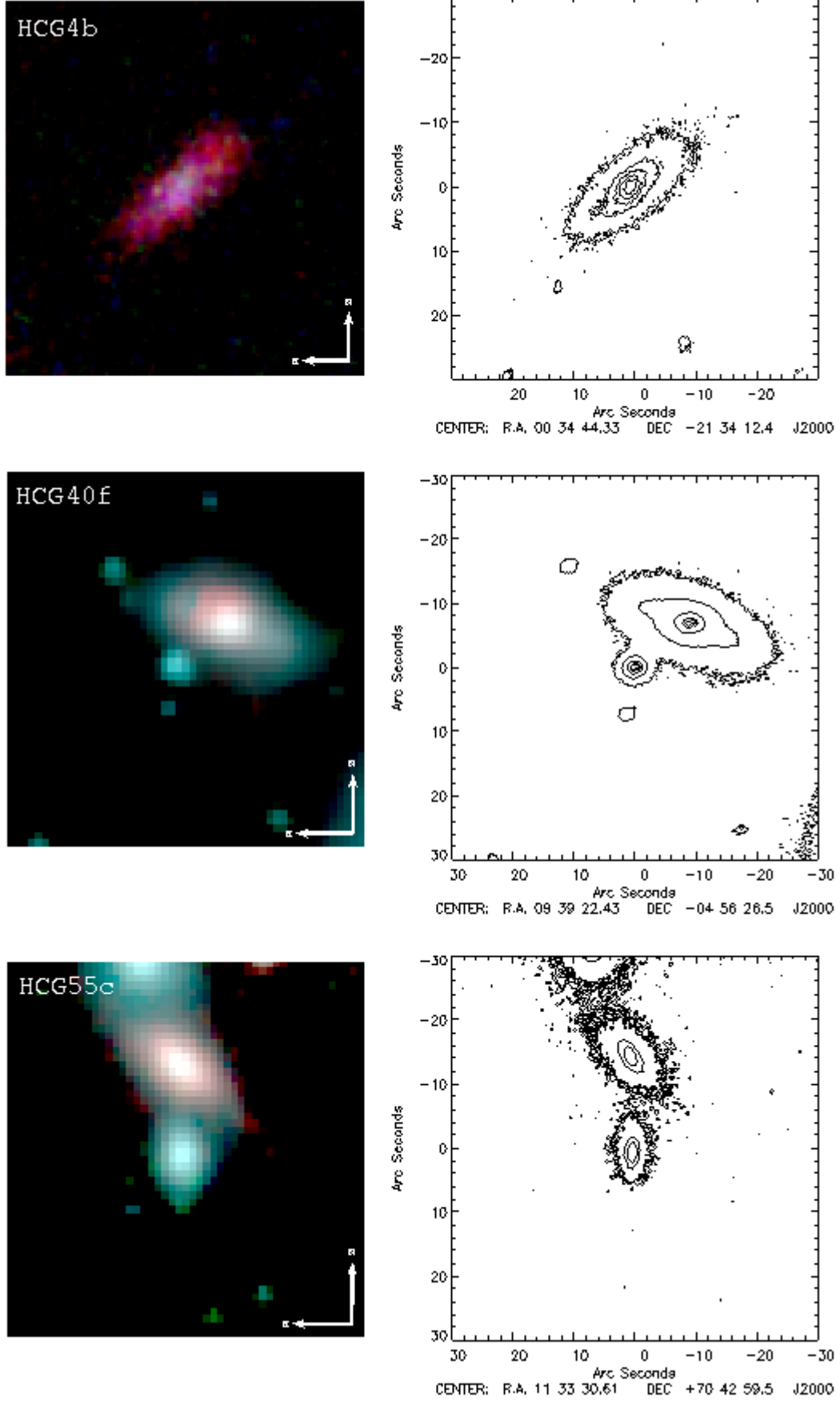


Fig. A.1. Left column: The “true color” images, created using the 3.6, 4.5 and 8.0 μ m Spitzer/IRAC mosaics, of the 10 galaxies discussed in Section 4.3. The images are aligned north-east and they are 1.5 \times 1.5 arcmin in size. **Right column:** Contour maps of the same fields observed in Ks-band with WIRC at the Palomar 5m telescope. The five contours correspond to 3, 5, 8, 10, and 30 σ . Since all images had similar exposure time the noise was $\sigma \sim 19.6$ mag arcsec $^{-2}$. For two galaxies, HCG68a and HCG100a, not imaged with WIRC we used the shallower Ks-band data from 2MASS ($\sigma = 15.7$ mag arcsec $^{-2}$).

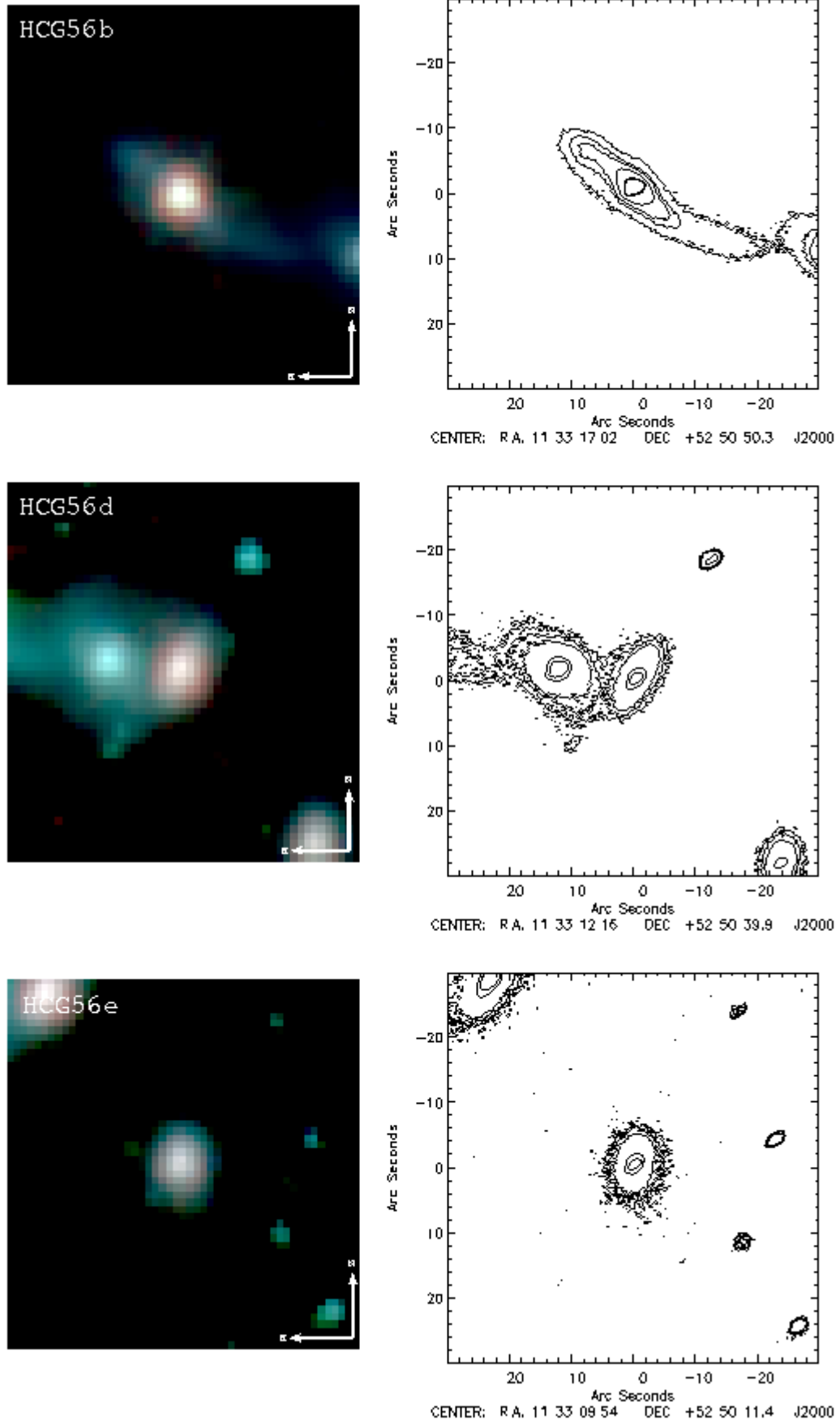


Fig. A.1. Continued

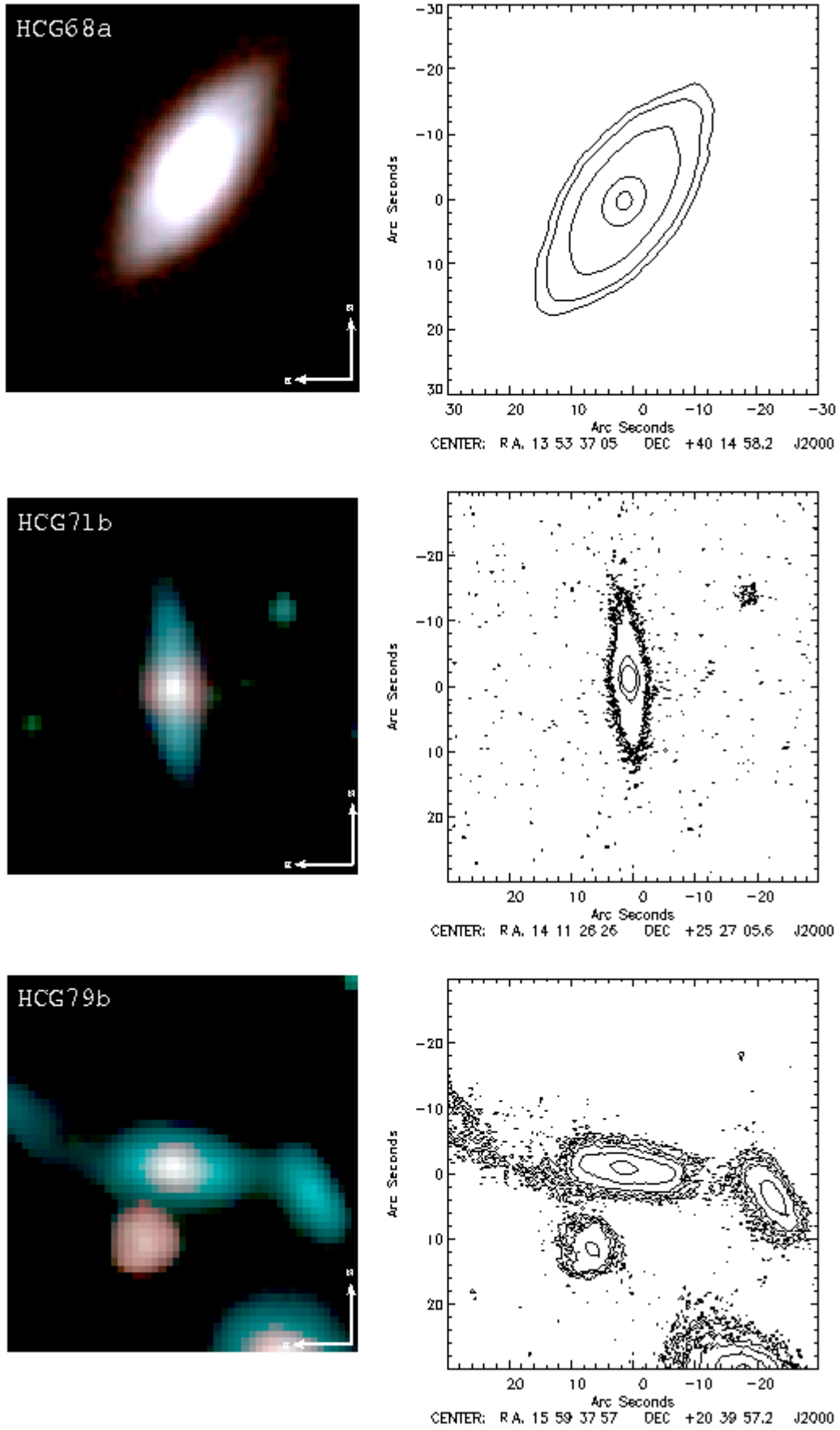
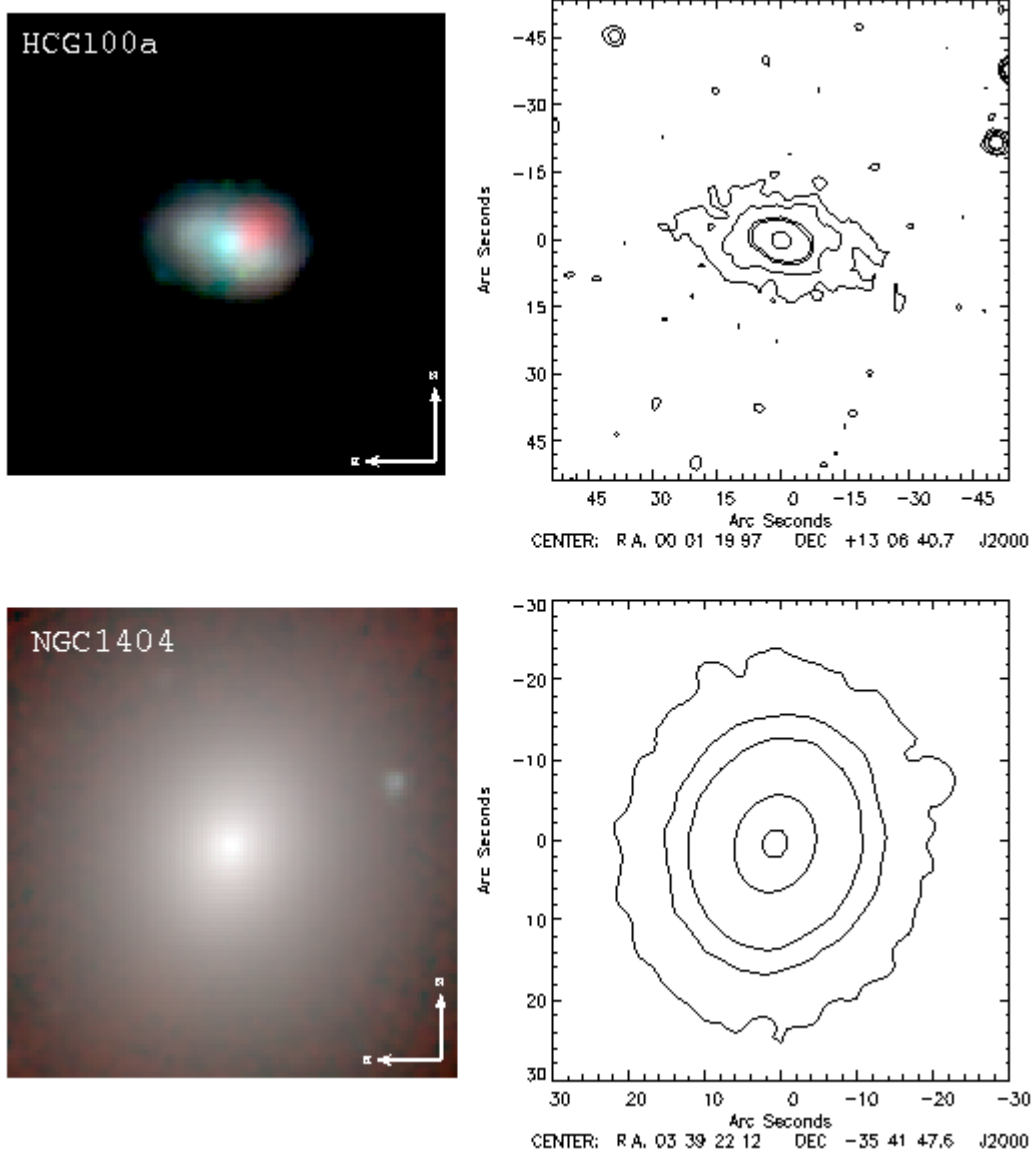


Fig. A.1. Continued

Table A.1. Properties of the 10 peculiar early-type HCG galaxies and the typical elliptical NGC 1404.

Galaxy	Type ^a	Optical feature	Nuclear type	SED type	$\tau_{V,obs}$	SFR $M_{\odot} \text{yr}^{-1}$	sSFR $\times 10^{-11} \text{yr}^{-1}$	(NUV-r) _{corr} [mag]	Proposed type
HCG 4d	E4	-	-	late-type	0.53	0.96	7.41	2.01	late-type
HCG 40f ^b	-	-	-	early-type	0.02	0.01	0.01	5.11	early-type
HCG 55c	E3	-	-	late-type	0.94	1.17	1.05	2.90	late-type
HCG 56b ^c	SB0	bar	Sy2	AGN dom.	1.34	1.69	4.79	2.04	-
HCG 56d	S0	-	Sy2	late-type	1.01	0.42	4.07	2.81	late-type
HCG 56e	S0	-	HII	late-type	0.89	0.19	5.37	2.78	late-type
HCG 68a	S0	-	AGN	early-type	0.02	0.31	0.46	3.81	early-type
HCG 71b	SB0	bar	HII	late-type	1.17	1.34	3.31	2.74	late-type
HCG 79b	S0	-	TO	late-type	0.99	0.10	0.35	2.95	late-type
HCG 100a	S0	-	TO	late-type	0.25	1.05	1.70	2.24	late-type
NGC 1404	E1	-	-	early-type	0.02	0.15	0.08	5.49	-

Notes. ^(a) Based on Hickson (1982). ^(b) Galaxy HCG40f is not detected at $24\mu\text{m}$, thus its SFR and sSFR are not well constrained. ^(c) Galaxy HCG56b emission is dominated by the presence of an AGN.


Fig. A.1. Continued

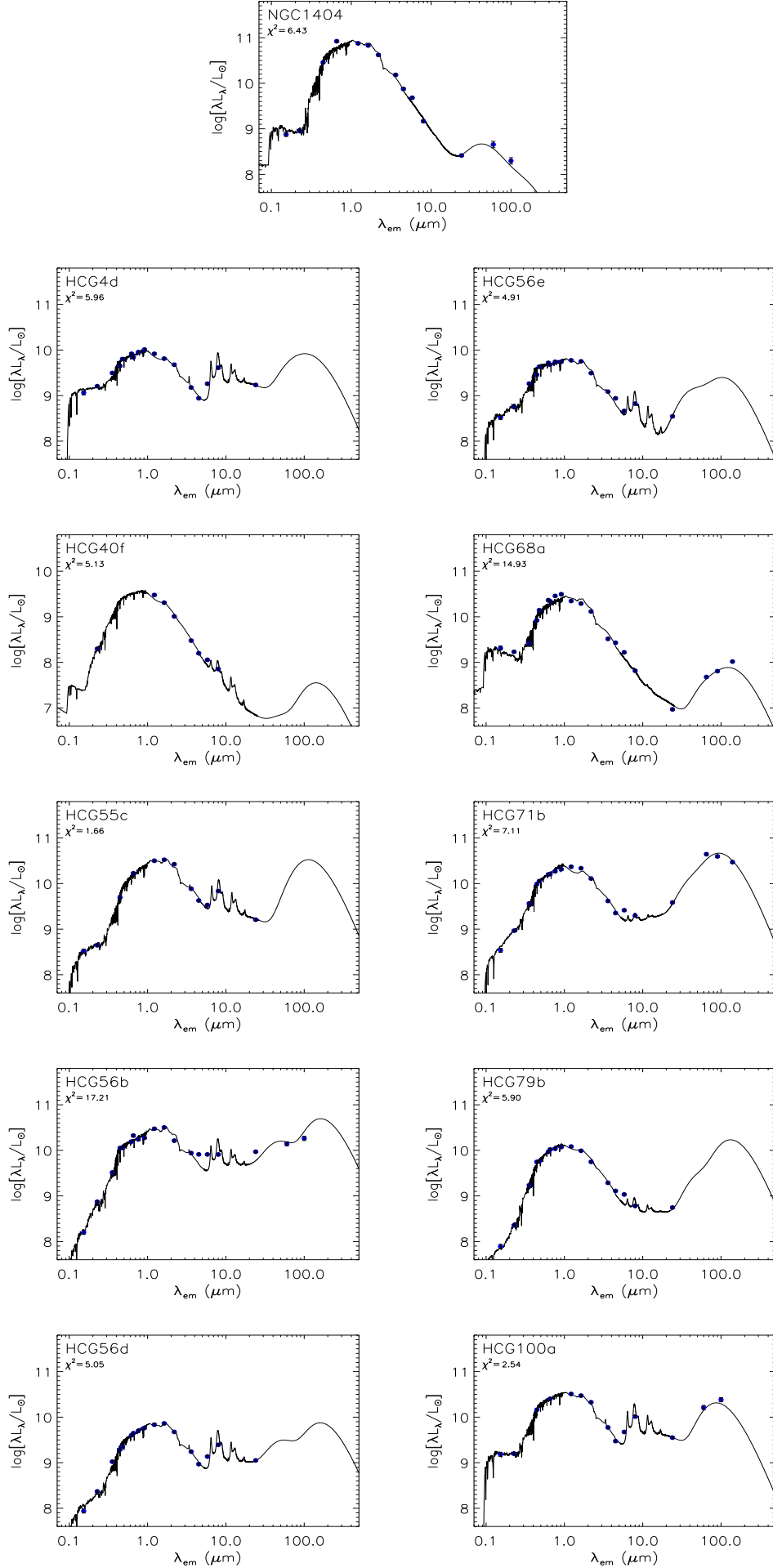


Fig. A.2. We display the observed SEDs (blue points) along with the da Cunha model fits (in black) of the 10 peculiar early-type galaxies mentioned in the Appendix. At the top panel we present the SED of a typical field elliptical galaxy, NGC 1404, for comparison. The name of each HCG galaxy along with the χ^2 of the model fit to the data is presented.